Multiscale Thermodynamics-Informed Neural Networks (MuTINN) towards fast and frugal inelastic computation of woven composite structures

M. El Fallaki Idrissi, Francis Praud, Fodil Meraghni, Francisco Chinesta, George Chatzigeorgiou

Multiscale Thermodynamics-Informed Neural Networks (MuTINN) towards Fast and Frugal Inelastic Computation of Woven Composite Structures.

M. El Fallaki Idrissi[a,b,*], F. Praud[a], F. Meraghni[a], F. Chinesta[b], G. Chatzigeorgiou[a]

[a] *Arts et Métiers Institute of Technology, CNRS, LEM3-UMR 7239, 4 rue Augustin Fresnel, 57078 Metz, France*
[b] *ESI Chair, Arts et Métiers Institute of Technology, CNRS, PIMM-UMR 8006, 151 Boulevard de l'Hôpital, 75013 Paris, France*

Abstract

The complex behavior of inelastic woven composites stems primarily from their inherent heterogeneity. Achieving accurate predictions of their linear and nonlinear responses, while considering their microstructures, appears feasible through the application of multi-scale modeling approaches. However, effectively incorporating these methodologies into real-scale applications, particularly within FE^2 analyses, remains challenging due to the significant computational requirements they entail. To overcome this issue, while considering the scale effects, this study introduces an alternative approach based on Artificial Neural Networks (ANNs) to perform a macroscopic surrogate model of composites. This model, referred to as Multiscale Thermodynamics Informed Neural Networks (MuTINN), is founded on thermodynamic principles and introduces specific quantities of interest that serve as internal

*Corresponding author.
Email address: mohammed.el_fallaki_idrissi@ensam.eu (M. El Fallaki Idrissi)

state variables at the macroscopic level. This captures efficiently the state and evolution laws governing the history-dependent behavior of these composites while retaining the thermodynamic admissibility and the physical interpretability of their overall responses. Moreover, to facilitate its numerical implementation within a FE code, a Meta-UMat has been developed, streamlining the application of multiscale FE-MuTINN approach for composite structure computations. The prediction capabilities of the proposed approach is demonstrated across the material scales, exemplified through diverse instances of woven composite structures. Theses applications account for anisotropic yarn damage and an elastoplastic polymer matrix behavior. The numerical results and the related comparison with experimental findings and FE computations demonstrate remarkable consistency across a wide range of non-proportional loading paths. This promises a potential solution to alleviate the computational challenges associated with multiscale simulations of large composite structures.

Keywords: Artificial Neural Networks, Thermodynamics, Multi-scale modeling, Woven composite structures, History-dependent behavior, Yarn damage, Random loading path.

1. Introduction

In recent years, there has been a significant and pronounced increase in the attention directed towards the realm of Artificial Intelligence (AI) (Glikson and Woolley, 2020). This surge is primarily attributed to three pivotal technological drivers: the accessibility of vast datasets, the rapid and continuous evolution of AI algorithms, and the exponential growth in computational capabilities (King and Roberts, 2018). Within the domain of engineering science, a growing acknowledgment is taking place among both researchers and industries regarding the vast potential of AI in tackling numerous challenges and driving significant advancements across an extensive spectrum of engineering fields (Salehi and Burgueño, 2018; Xu et al., 2021; Chinesta and Cueto, 2022). Moreover, traditionally, materials science has been based on three fundamental paradigms: the first centered on empirical and experimental testing, the second revolved around the application of physics and thermodynamics principles to create constitutive models, and the third concentrated on the realm of computer simulations. More recently, a fourth paradigm has emerged, characterized by data-driven scientific methodologies and the integration of Machine Learning (ML) techniques (Agrawal and Choudhary, 2016; Kirchdoerfer and Ortiz, 2016; Ibanez et al., 2018; Wei et al., 2019). Among these paradigms, the fourth one holds significant promise, particularly given the ongoing advancements in data mining technology and artificial intelligence. It has the potential to integrate the other three paradigms, enabling a more seamless alignment in terms of experimental exploration, theoretical comprehension, and computational simulation. In this context, AI techniques have garnered considerable attention as valuable tools for ex-

pediting the exploration and design of novel materials with precisely tailored properties, discovering material constitutive models, accelerating computational simulation, improving manufacturing characterization, and facilitating the optimization of design processes (Frank et al., 2020; Morgan and Jacobs, 2020).

Although composite materials find extensive utility across diverse engineering and industrial domains, their widespread incorporation is frequently hindered by challenges, notably the accurate prediction of their overall mechanical response taking into account the characteristics of their microstructure. Over the preceding years, a multitude of multiscale techniques including analytical, semi-analytical, and numerical methods have been developed (Eshelby, 1956; Moulinec and Suquet, 1998; Castaneda and Suquet, 1997; Castaneda, 2002; Chatzigeorgiou et al., 2022). These methods aim at providing a thorough understanding of the mechanisms and phenomena taking place across various scales, spanning from the micro to the macro level. Nevertheless, even with the ongoing progress in computing capabilities, multiscale numerical simulation of large-scale composite structures (e.g. FE^2 (Feyel and Chaboche, 2000; Tikarrouchine et al., 2018, 2021)) remains an arduous task. Confronting this challenge head-on, composite materials have gained prominence in two key domains: Model Order Reduction (MOR) techniques—such as Transformation Field Analysis (TFA) (Dvorak and Benveniste, 1992; Dvorak et al., 1994b,a; Chatzigeorgiou and Meraghni, 2019; Barral et al., 2020), Self-Clustering Analysis (SCA) (Liu et al., 2016, 2018), and Proper Generalized Decomposition (PGD) (Chinesta et al., 2010, 2011; Metoui et al., 2018; El Fallaki Idrissi et al., 2022)— and AI techniques, including machine learn-

ing and deep learning (Ghavamian and Simone, 2019; Wu et al., 2020; Liu et al., 2021; Jiang et al., 2023). Through the integration of these methodologies, it becomes possible to perform a concurrent two-scale framework without the necessity for a complete FE^2 implementation. Nevertheless, dealing with materials exhibiting history- or time-dependent behaviors, where the stress prediction depends not only on the current stress and strain states, but also on the entire loading history, it can indeed present a challenging task. In this given context, significant efforts are currently being directed towards the development of specialized machine learning and deep learning tools (Wu et al., 2023; Liu et al., 2019). These tools are meticulously designed to address the complex multiscale nature along with the inelastic behaviors that are inherently present within these materials. In a more recent development, a technique known as Deep Material Networks (DMN) has emerged for multiscale material modeling (Liu et al., 2019; Gajek et al., 2021, 2022). This approach builds upon the concept of material networks, employing a collection of interconnected basic elements specifically chosen for their simplicity and analytical homogenization. Although it demonstrates proficiency in describing diverse microstructure responses within the realms of both elastic and plastic behavior, it faces significant hurdles when confronted with highly intricate microstructures, such as woven-reinforcement composites. Alternative methodologies have been developed, leveraging Recurrent Neural Networks (RNNs) and incorporating well-established components such as Long Short-Term Memory (LSTM) and Gated Recurrent Units (GRU) (Ghavamian and Simone, 2019; Wu et al., 2020; Chen et al., 2021; Ghane et al., 2023; El Said, 2023). These algorithmic frameworks act as mecha-

nisms that convert input sequences into desired output sequences, specifically in our context, corresponding to strain and stress tensors. Although numerous studies have showcased the effectiveness of RNN-based models in predicting history-dependent behaviors using only stress-strain sequences without requiring knowledge of Internal State Variables (ISVs), their widespread adoption in multiscale modeling encounters several challenges. These stem primarily from the significant amount of data required to effectively train their complex architecture. Additionally, they face limitations in making accurate predictions beyond the training dataset, and they often suffer from a lack of physical meaning and interpretability. This lack of interpretability is a common issue with ANNs, as they are often perceived as *black boxes*, leading to uncertainty about their inner workings and, consequently, their predictive capabilities in the field of material science. This opacity could potentially pose significant risks when applied to constitutive modeling for investigating extreme events, especially when dealing with complex unseen loading paths. That is why, significant endeavors have been undertaken to reduce instances of inconsistent results by introducing constraints derived from the principles of physics (Karniadakis et al., 2021; Cueto and Chinesta, 2023; Eghbalian et al., 2023), like the well-established Physics-Informed Neural Networks (PINN). This, in turn, enhances the stability and accuracy of the models during implementation and reduces the imperative for extensive training datasets. Based on the PINN concept, a novel form of artificial neural networks known as TANN (Thermodynamics-based Artificial Neural Networks) has been devised in (Masi et al., 2021). This model integrates thermodynamic principles into ANNs, allowing for the generation of predic-

tions that are thermodynamically consistent not only for the training dataset (seen loading paths) but also for the test dataset (unseen loading paths) (Masi et al., 2021). TANN receive inputs including current stress, strain and ISVs, as well as strain increments. In turn, the model produces outputs such as free energy, dissipation rate, and updated ISVs and stress. Consequently, during the training process of TANN, it is imperative to provide data for all the aforementioned fields. This model has been recently employed to perform two-scale simulations of inelastic lattice microstructures (Masi and Stefanou, 2022). It successfully identifies the ISVs that describe the inelastic deformation within the intricate microstructural fields using an Encoder-Decoder model.

Taking inspiration from the PINN and TANN models, this paper introduces a novel approach referred to as Multiscale Thermodynamics-Informed Neural Networks (MuTINN). Within this model, two consecutive neural networks are employed to formulate macroscopic constitutive relationships for inelastic heterogeneous materials, while integrating fundamental thermodynamics background. The first network captures the evolution law, while the second delineates the state law. The incorporation of thermodynamic principles into ANNs not only enhances their performance but also significantly reduces the need for extensive training data, as it eliminates the necessity to capture the underlying patterns of thermodynamic laws. Moreover, to preserve the physical characteristics of the input and output variables, we introduce specific quantities of interest act as ISVs at the macroscale. These quantities are computed by averaging specific ISVs defined at the microscale, corresponding to the scale of the unit cell. Consequently, MuTINN eliminates

the necessity for neural networks with memory functions, such as RNNs, by separately tracking these quantities of interest throughout any given loading path.

The efficiency and the predictability of MuTINN approach has been verified by applying it to woven composites with history-dependent behavior involving an elastoplastic polymer with an anistropic damage within the yarns. Notably, our approach consistently delivers exceptional performance under various in-plane loading conditions, validating its robustness, precision, and adherence to thermodynamic principles. Additionally, a Meta-UMat has been developed to simplify the integration of MuTINN based ANN models into commercial finite element software. Subsequently, multiscale simulations are conducted, employing finite element analysis at the macroscale and MuTINN at the microscale, to examine different woven composite structures. These examples demonstrate significant gains in accuracy and computational time savings without sacrificing thermodynamic consistency of the results.

The manuscript is organized as follows: In Section 2, we provide a brief introduction to the composite materials under investigation, including microstructure geometry and the local constitutive models of both yarns and matrix. We also discuss the theoretical framework of periodic homogenization, which serves as the basis for performing high-fidelity simulations used to train the proposed model. Section 3 is dedicated to the presentation of the quantities of interest, as well as the MuTINN model architecture, a significant contribution in our research. Section 4 covers the discussion of the training, validation, and testing processes of the MuTINN model, including data generation and optimization. In the same section, we showcase

the MuTINN model's predictive capabilities under unseen random loading conditions. Section 5, presents the integration of MuTINN into a FE code towards structure computations. Then, the FE-MuTINN is used to perform load-unload tests at the unit-cell scale and the obtained results are compared with FE-based periodic homogenization and experimental data for different laminate orientations, including $\pm[0°]_s$, $\pm[30°]_s$, and $\pm[45°]_s$ laminates. In the same section, FE-MuTINN is applied to a large-scale composite structure (Open-Hole structure) with different fabric orientations and the results are also compared with experimental data. Lastly, in Section 6, we conclude the manuscript by summarizing the essential findings of our research and outlining potential future directions.

2. Woven composite: Microstructure, local thermodynamic models and periodic homogenization

2.1. Woven composite architecture

The framework established within this study can be used effectively across an extensive spectrum of inelastic composite materials. This spectrum encompasses diverse forms of reinforcement, including long and short fibers, as well as both woven and non-woven fabrics. To underscore its adaptability and versatility, our primary focus will be directed towards an in-depth exploration of thermoplastic-based woven composites. In particular, we will place special emphasis on those consisting of Polyamide 6-6 (PA66) as the matrix material and employing a 2-2 twill weave architecture for reinforcement. These composites are widely used in various commercial and industrial applications due to their numerous attractive properties such as stability, smoothness,

and drape (Strong, 2008). Notably, these characteristics contribute to an improved formability, enabling them to conform to complex surface geometries and curvatures. In addition, they demonstrate remarkable effectiveness in enhancing structural integrity across multiple orientations within a single layer when compared to unidirectional (UD) composites (Aliabadi, 2015).

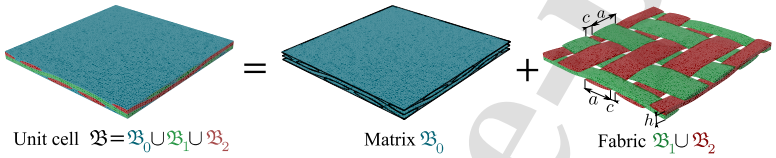

Figure 1: Woven Thermoplastic Composite Unit Cell ($\mathfrak{B}$) with 2-2 Twill Fabric Reinforcement: Key Parameters - Weft and Warp Width (a), Yarn Gap (c), Fabric Thickness (h).

In the context of homogenization, we take into account the periodic nature of the woven composite microstructure by defining the microscopic problem using a Unit Cell (UC). This unit cell serves as a fundamental representation of the smallest repeating element within the microstructure. We refer to this element as $\mathfrak{B}$, which includes distinct phases, as illustrated in Figure 1. Specifically, it comprises the matrix phase, identified as sub-domain $\mathfrak{B}_0$, along with the weft and warp yarn phases, referred to as sub-domains $\mathfrak{B}_1$ and $\mathfrak{B}_2$, respectively. Figure 1 also illustrates the geometry of the UC, which is defined by a specific set of parameters. These parameters include the yarn width, represented as a, the fabric thickness denoted as h, and the gap between adjacent yarns labeled as c. The specific numerical values for these parameters of the analyzed microstructure can be found in Table 1. It is noteworthy that the same woven composite material has been employed in prior research efforts, as referenced in (Tikarrouchine et al., 2021; Praud,

2018).

Table 1: Geometric parameter values for the 2-2 twill weave composite.

Parameter	Description	Value	Unit
a	Yarn width	3.46	mm
h	Fabric thickness	0.45	mm
c	Gap between two adjacent yarns	0.29	mm

2.2. Local constitutive behaviors

The investigated woven composite material exhibits an inelastic and path-dependent behavior, which incorporates distinct local constitutive models for both yarns and matrix materials. These models, as presented in (Praud et al., 2017a,b), primarily focus on exploring the complex and time-dependent characteristics of the matrix, which involves a viscoelastic-viscoplastic model coupled with a ductile damage. In this study, for the sake of simplicity, we model its behavior using a conventional elasto-plastic constitutive model with isotropic hardening, as described in previous works (Chaboche, 1989, 2008). Consequently, the state laws governing the matrix material are based on the following form of the Helmholtz free energy density:

$$\Psi(\boldsymbol{\varepsilon}, \boldsymbol{\varepsilon}_p, p) = \frac{1}{2}(\boldsymbol{\varepsilon} - \boldsymbol{\varepsilon}_p) : \mathbb{C}_e : (\boldsymbol{\varepsilon} - \boldsymbol{\varepsilon}_p) + \int_0^p R(\xi)\ \mathrm{d}\xi, \tag{1}$$

where $\mathbb{C}_e$ represents fourth-order stiffness tensors traditionally established for bulk isotropic materials using the Young's modulus E and the Poisson's ratio ν. On the other hand, $R(\xi)$ represents the hardening function, which is expressed here as an exponential linear function:

$$R(p) = Q_1\big(1 - \exp(-bp)\big) + Q_2 p, \tag{2}$$

Table 2: Parameters of the elasto-plastic model identified for thermoplastic matrix (PA66).

Feature	Parameter	Value	Unit
Young's modulus	E	2 074	MPa
Poisson's ratio (standard value)	ν	0.3	-
Yield threshold	σ_y	14	MPa
Hardening parameters	Q_1	30	MPa
	b	160	-
	Q_2	260	MPa

where Q_1, Q_2 and b are the hardening parameters.

As depicted in Table 2, it is imperative to underscore that the parameters for the elasto-plastic matrix model have been determined based on the results of a monotonically loaded test. This test data is sourced from prior research on unfilled PA66, as documented in (Praud et al., 2017a).

Referring to Table 3, it can be observed that the total strain, denoted as $\boldsymbol{\varepsilon}$, serves as an external state variable, while the plastic strain $\boldsymbol{\varepsilon}_p$ and the equivalent plastic strain p function as internal state variables. The mathematical expressions describing these state variables and their associated counterparts, along with their corresponding evolution laws ($\dot{\boldsymbol{\varepsilon}_p}$ and $\dot{p}$), as well as the yield criterion function f, can be summarized in Table 3:

Observable state variable	Associated variable (state law)
$\boldsymbol{\varepsilon}$	$\boldsymbol{\sigma} = \dfrac{\partial \Psi}{\partial \boldsymbol{\varepsilon}} = \mathbb{C}_{\boldsymbol{e}} : (\boldsymbol{\varepsilon} - \boldsymbol{\varepsilon}_{\boldsymbol{p}})$

Internal state variables	Associated variables	Evolution laws
$\boldsymbol{\varepsilon}_{\boldsymbol{p}}$	$-\boldsymbol{\sigma} = \dfrac{\partial \Psi}{\partial \boldsymbol{\varepsilon}_{\boldsymbol{p}}}$	$\dot{\boldsymbol{\varepsilon}}_{\boldsymbol{p}} = \dfrac{\partial F}{\partial \boldsymbol{\sigma}} \dot{\lambda} = \boldsymbol{\Lambda}(\boldsymbol{\sigma}) \dot{p}$
p	$R = \dfrac{\partial \Psi}{\partial p} = R(p)$	$\dot{p} = -\dfrac{\partial F}{\partial R} \dot{\lambda} = \dot{\lambda}$

Multiplier	Activation of the multiplier
$\lambda = p$	$f = \mathrm{eq}(\boldsymbol{\sigma}) - R(p) - \sigma_y \leq 0 \quad \begin{cases} f < 0, & \dot{\lambda} = 0 \\ f = 0, & \dot{\lambda} > 0 \end{cases}$

Table 3: Summary of the constitutive equations for the matrix sub-domain $\mathfrak{B}_0$.

In contrast, the yarns demonstrate a linear elastic response when subjected to forces along their longitudinal axis until they eventually experience brittle failure. Conversely, when forces are applied in the transverse direction, their behavior deviates from linearity, displaying inelastic properties. This inelastic response stems from the gradual emergence of damage, primarily induced by the diffuse growth of micro-cracks originating at the interfaces between the fibers and the matrix due to debonding. Subsequently, these micro-cracks propagate through a coalescence process. This behavior can be described using the hybrid micromechanical-phenomenological constitutive model developed in (Praud et al., 2017b) and schematically illustrated in Figure 2. Yarns are conceptualized as unidirectional long fibers packed densely within a matrix. Their behavior is characterized using a Representative Volume Element (RVE) that incorporates a micro-crack density γ_c. This density is employed to define an anisotropic damage fourth-order ten-

sor denoted as $\mathbb{D}(\gamma_c)$, which effectively diminishes the initially transversely isotropic stiffness tensor $\mathbb{C}_0$. Consequently, due to the non-closure effect of these micro-cracks, damage often leads to observable permanent deformations. These deformations are phenomenologically represented by an inelastic strain tensor, denoted as $\boldsymbol{\varepsilon}_s$. Hence, the state laws governing yarns are based on the specific form of the Helmholtz free energy density as follows:

$$\Psi(\boldsymbol{\varepsilon}, \boldsymbol{\varepsilon}_s, \gamma_c) = \frac{1}{2}(\boldsymbol{\varepsilon} - \boldsymbol{\varepsilon_s}) : \left[\mathbb{C}_0 - \mathbb{D}(\gamma_c)\right] : (\boldsymbol{\varepsilon} - \boldsymbol{\varepsilon_s}), \tag{3}$$

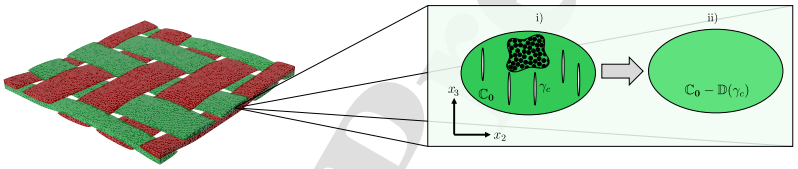

Figure 2: Schematic illustration of micromechanical description of yarn damage: a Representative Volume Element (RVE) of yarn incorporating micro-crack density γ_c and its role in defining an anisotropic fourth-order damage tensor $\mathbb{D}(\gamma_c)$ to reduce the initially transversely isotropic stiffness tensor $\mathbb{C}_0$.

More detailed information regarding the behavior of yarns can be located in Table 4, where the principal constitutive equations governing their behavior are outlined. Therefore, readers can refer to the following citations for further information (Tikarrouchine et al., 2021; Praud et al., 2021; Praud, 2018).

Observable state variable	Associated variable (state law)	
$\boldsymbol{\varepsilon}$	$\boldsymbol{\sigma} = \dfrac{\partial \Psi}{\partial \boldsymbol{\varepsilon}} = \left[\mathbb{C}_0 - \mathbb{D}(\gamma_c)\right] : (\boldsymbol{\varepsilon} - \boldsymbol{\varepsilon}_s)$	
Internal state variables	**Associated variables**	**Evolution laws**
$\boldsymbol{\varepsilon}_s$	$-\boldsymbol{\sigma} = \dfrac{\partial \Psi}{\partial \boldsymbol{\varepsilon}_s}$	$\dot{\boldsymbol{\varepsilon}}_s = \dfrac{\partial F}{\partial \boldsymbol{\sigma}} \dot{\lambda} = \boldsymbol{\Lambda}_s(\boldsymbol{\sigma}) \dot{\gamma}_c$
γ_c	$-Y_c = \dfrac{\partial \Psi}{\partial \gamma_c}$	$\dot{\gamma}_c = \dfrac{\partial F}{\partial Y_c} \dot{\lambda} = \dot{\lambda}$
Micromechanical variables	**Local mean strain and stress in the virgin part**	
$\boldsymbol{\varepsilon}_0$	$\boldsymbol{\varepsilon}_0 = \mathbb{A}_0(\gamma_c) : (\boldsymbol{\varepsilon} - \boldsymbol{\varepsilon}_s)$	
$\boldsymbol{\sigma}_0$	$\boldsymbol{\sigma}_0 = \mathbb{C}_0 : \mathbb{A}_0(\gamma_c) : (\boldsymbol{\varepsilon} - \boldsymbol{\varepsilon}_s)$ or $\boldsymbol{\sigma}_0 = \mathbb{B}_0(\gamma_c) : \boldsymbol{\sigma}$	
H_c	$H_c = \sqrt{\boldsymbol{\sigma}_0 : \mathbb{H} : \boldsymbol{\sigma}_0}$	
Multiplier	**Activation of the multiplier**	
$\lambda = \gamma_c$	$f = g(H_c) - \gamma_c \leq 0 \quad \begin{cases} f < 0, & \dot{\lambda} = 0 \\ f = 0, & \dot{\lambda} > 0 \end{cases}$	

Table 4: Summary of the constitutive equations for the yarns sub-domains weft yarns $\mathfrak{B}_1$ and warp yarns $\mathfrak{B}_2$.

2.3. Non-linear periodic homogenization

Generating a dataset for training and evaluating MuTINN necessitates employing high-fidelity simulations that can yield remarkable accuracy and consistency in trained ANNs predictions. Therefore, given the periodic nature of the microstructure, employing periodic homogenization-based multiscale approaches (Figure 3) seems to be an optimal framework for this task. This methodology typically involves establishing a robust link between the microscopic and macroscopic scales, ensuring the reliable representation of the system's behavior across different levels of detail. This is usually done

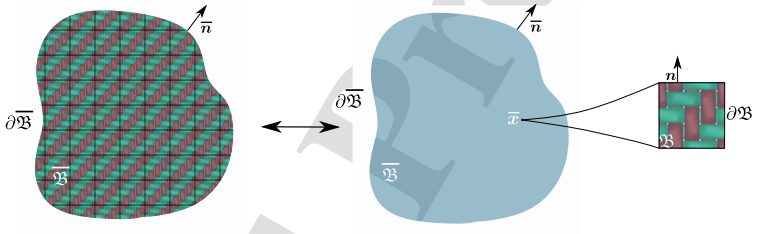

Figure 3: Multiscale Modeling (Periodic Homogenization): Transition from Woven Composite Material (Left) to an Equivalent Homogenized Medium (Middle) with a detailed Unit Cell (Right).

by averaging the microscopic stress, strain and Helmholtz free energy over the whole unit cell domain $\mathfrak{B}$ as follow:

$$\overline{\boldsymbol{\sigma}}(t) = \frac{1}{V}\int_{\mathfrak{B}} \boldsymbol{\sigma}(\boldsymbol{x},t)\ \mathrm{d}V, \tag{4a}$$

$$\overline{\boldsymbol{\varepsilon}}(t) = \frac{1}{V}\int_{\mathfrak{B}} \boldsymbol{\varepsilon}(\boldsymbol{x},t)\ \mathrm{d}V, \tag{4b}$$

and

$$\overline{\Psi}(t) = \frac{1}{V}\int_{\mathfrak{B}} \Psi(\boldsymbol{x},t)\ \mathrm{d}V, \tag{4c}$$

where V represents the volume of the UC domain $\mathfrak{B}$.

As previously examined in existing literature (Suquet, 1987), the concept of Periodic Homogenization hinges on the underlying assumption of periodicity, which dictates the form of the displacement field $\boldsymbol{u}$ within the unit cell as follows:

$$\boldsymbol{u}(\boldsymbol{x},t) = \overline{\boldsymbol{\varepsilon}}(t)\cdot\boldsymbol{x} + \tilde{\boldsymbol{u}}(\boldsymbol{x},t) + \boldsymbol{u}_0(t), \qquad \forall \boldsymbol{x}\in\mathfrak{B}. \tag{5}$$

This equation consists of three key components: firstly, an affine part represented as $\overline{\boldsymbol{\varepsilon}}\cdot\boldsymbol{x}$; secondly, a periodic fluctuation denoted as $\tilde{\boldsymbol{u}}$; and lastly, a possible contribution from rigid body motion, denoted as $\boldsymbol{u}_0$. It is worth noting that the periodic nature of $\tilde{\boldsymbol{u}}$ leads to the definition of Periodic Boundary Conditions (PBCs) as follows:

$$\boldsymbol{u}(\boldsymbol{x}_+,t) - \boldsymbol{u}(\boldsymbol{x}_-,t) = \overline{\boldsymbol{\varepsilon}}(t)\cdot(\boldsymbol{x}_+ - \boldsymbol{x}_-), \qquad \forall \boldsymbol{x}_+,\boldsymbol{x}_-\in\partial\mathfrak{B}. \tag{6}$$

where $\boldsymbol{x}+$ and $\boldsymbol{x}-$ denote points situated at opposite and symmetrical positions along the borders of the unit cell, denoted as $\partial\mathfrak{B}$

Therefore, it becomes feasible to acquire the macroscopic stress-strain behavior along a specified loading path by solving local equilibrium using periodic boundary conditions, all while considering the relationships involved in transitioning between scales. In this work, for the interest of simplification, and without sacrificing generality, we exclusively focus on in-plane macroscopic stress conditions. This implies that the values of $\overline{\sigma}_{33}$, $\overline{\sigma}_{13}$, and $\overline{\sigma}_{23}$ are assumed to be zero, while only the remaining components come into play.

3. MuTINN approach and variables

3.1. The quantities of interest $\overline{\boldsymbol{v}}$

MuTINN model aims at developing a phenomenological framework to accurately describe the inelastic behavior of RVEs. Unlike relying on memory-based Artificial Neural Networks such as RNN (Danoun et al., 2022; El Said, 2023), MuTINN eliminates this requirement but necessitates the inclusion of additional variables to effectively capture the history-dependent nature of nonlinear material behavior. In the context of homogenization theories, such as variables are originally defined at the microscale as ISVs and are associated with individual microscopic behaviors. However, the inclusion of such ISVs can impose a substantial computational burden during model training, mainly due to the increased number of input dimensions. To address this challenge, our methodology introduces specialized variables known as "quantities of interest ($\overline{\boldsymbol{v}}$)". These quantities are defined at a macroscopic level and play a crucial role in the formulation of the MuTINN model. They are derived by averaging specific ISVs within the domains of the matrix $\mathfrak{B}_0$, weft yarns $\mathfrak{B}_1$, and warp yarns $\mathfrak{B}_2$. They offer a valuable physical interpretation by tracking metrics such as damage density and accumulated plastic strain.

For the matrix phase analysis, we define four crucial quantities of interest, denoted as $\overline{v}_1$, $\overline{v}_2$, $\overline{v}_3$, and $\overline{v}_4$. These variables represent the averages of the accumulated plastic strain (p) within the matrix domain, as well as the averages of the in-plane plastic strain components, namely $\varepsilon_{p_{11}}$, $\varepsilon_{p_{22}}$, and $2\varepsilon_{p_{12}}$, respectively. Their mathematical expressions are detailed as follows:

$$\forall \boldsymbol{x} \in \mathfrak{B}_0 \begin{cases} \overline{v}_1(t) = \dfrac{1}{V_0} \displaystyle\int_{\mathfrak{B}_0} p(\boldsymbol{x}, t)\ \mathrm{d}V, \\ \overline{v}_2(t) = \dfrac{1}{V_0} \displaystyle\int_{\mathfrak{B}_0} \varepsilon_{p_{11}}(\boldsymbol{x}, t)\ \mathrm{d}V, \\ \overline{v}_3(t) = \dfrac{1}{V_0} \displaystyle\int_{\mathfrak{B}_0} \varepsilon_{p_{22}}(\boldsymbol{x}, t)\ \mathrm{d}V, \\ \overline{v}_4(t) = \dfrac{1}{V_0} \displaystyle\int_{\mathfrak{B}_0} 2\varepsilon_{p_{12}}(\boldsymbol{x}, t)\ \mathrm{d}V, \end{cases} \tag{7}$$

where V_0 represents the volume occupied by matrix phase.

Although the same internal state variables, such as γ_c, $\varepsilon_{s_{22}}$, and others, are defined for both warp and weft yarns, their evolution during the loading process may differ between warp and weft yarns, due to the anisotropic nature of the yarn damage. In fact, it depends on whether the load is in the transversal or longitudinal direction. However, in the transition from a high-dimensional representation (microscale ISVs) to a low-dimensional one (macroscale quantities of interest) while minimizing information loss, two sets of quantities of interest have been defined for yarns. Specifically, we have ($\overline{v}_5$, $\overline{v}_6$, and $\overline{v}_7$) for weft yarns and ($\overline{v}_8$, $\overline{v}_9$, and $\overline{v}_{10}$) for warp yarns. Their respective mathematical expressions are presented as follows:

$$\forall \boldsymbol{x} \in \mathfrak{B}_1 \begin{cases} \overline{v}_5(t) = \dfrac{1}{V_1} \displaystyle\int_{\mathfrak{B}_1} \gamma_c(\boldsymbol{x}, t)\ \mathrm{d}V, \\ \overline{v}_6(t) = \dfrac{1}{V_1} \displaystyle\int_{\mathfrak{B}_1} \varepsilon_{s_{22}}(\boldsymbol{x}, t)\ \mathrm{d}V, \\ \overline{v}_7(t) = \dfrac{1}{V_1} \displaystyle\int_{\mathfrak{B}_1} 2\varepsilon_{s_{12}}(\boldsymbol{x}, t)\ \mathrm{d}V, \end{cases} \tag{8}$$

$$\forall \boldsymbol{x} \in \mathfrak{B}_2 \begin{cases} \overline{v}_8(t) = \dfrac{1}{V_2} \displaystyle\int_{\mathfrak{B}_2} \gamma_c(\boldsymbol{x}, t)\ \mathrm{d}V, \\ \overline{v}_9(t) = \dfrac{1}{V_2} \displaystyle\int_{\mathfrak{B}_2} \varepsilon_{s_{22}}(\boldsymbol{x}, t)\ \mathrm{d}V, \\ \overline{v}_{10}(t) = \dfrac{1}{V_2} \displaystyle\int_{\mathfrak{B}_2} 2\varepsilon_{s_{12}}(\boldsymbol{x}, t)\ \mathrm{d}V, \end{cases} \tag{9}$$

where V_1 and V_2 represent the volumes of the weft and warp yarns, respectively.

As indicated by the equations 8 and 9, only the $\varepsilon_{s_{22}}$ and $2\varepsilon_{s_{12}}$ components of the anelastic strain tensor are taken into account, as these components are active and evolve with the microcrack density during in-plane loading. In fact, microcracks are forced to propagate in a plane parallel to the fiber direction $\vec{x}_1$, as shown in Figure 2, which illustrates the micromechanical description of yarn damage.

3.2. MuTINN architecture

The Multiscale Thermodynamics-Informed Neural Network (MuTINN) is an ANN-based model built upon the principles of thermodynamics. It has been designed for the analysis of inelastic woven composites, with the potential for application to various inelastic microstructures. As illustrated in Figure 4, MuTINN's architecture consists of two distinct ANNs, each with its unique purpose. The first ANN is specifically designed to describe the evolution law, taking as inputs the current macroscopic strain components ($\overline{\boldsymbol{\varepsilon}}^n = [\overline{\varepsilon}^n_{11}, \overline{\varepsilon}^n_{22}, 2\overline{\varepsilon}^n_{12}]^{\mathrm{T}}$), the current quantities of interest ($\overline{\boldsymbol{v}}^n = [\overline{v}^n_1, \ldots, \overline{v}^n_{10}]^{\mathrm{T}}$), and the macroscopic strain increment ($\Delta\overline{\boldsymbol{\varepsilon}}^{n+1}$). Subsequently, it calculates the corresponding increment ($\Delta\overline{\boldsymbol{v}}^{n+1}$). Conversely, the second ANN, known as the state law model, takes inputs consisting of the updated macroscopic

strain ($\overline{\boldsymbol{\varepsilon}}^{n+1}$) and the updated quantities of interest ($\overline{\boldsymbol{v}}^{n+1}$), and predicts the Helmholtz free energy ($\overline{\Psi}^{n+1}$) as its output. Then, an automatic differentiation is used to partially differentiate the predicted Helmholtz free energy with respect to the inputs. This process is performed to determine both the macroscopic stress components ($\overline{\boldsymbol{\sigma}}^{n+1} = [\overline{\sigma}_{11}^{n+1}, \overline{\sigma}_{22}^{n+1}, \overline{\sigma}_{12}^{n+1}]^{\mathrm{T}}$) and the dissipation ($\dot{\overline{\Phi}}^{n+1}$). Within the MuTINN framework, the dissipation is calculated solely for ensuring consistent thermodynamic predictions. To this end, a penalty function has been incorporated to promote solutions with positive dissipation preserving hence the thermodynamics admissibility. It is worth noting that in this particular context, as the behavior being examined is time-independent, the dissipation is computed using a fixed time increment of 1 ($\Delta \mathrm{t} = 1$).

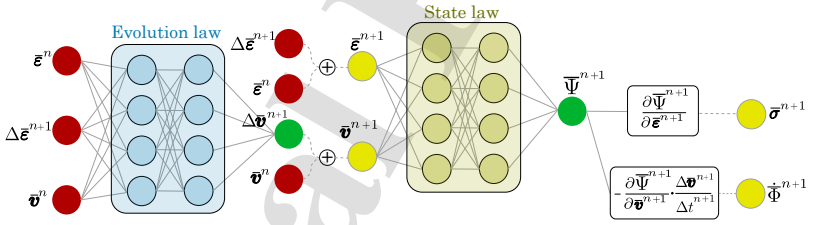

Figure 4: Multiscale Thermodynamics-Informed Neural Networks (MuTINN) architecture.

To train the MuTINN model, we define a loss function denoted as L, which consists of the sum of three individual loss functions ($L_{\overline{\boldsymbol{v}}}$, $L_{\overline{\Psi}}$, $L_{\overline{\boldsymbol{\sigma}}}$), accompanied by a penalty function $P_{\dot{\overline{\Phi}}}$, as expressed in the following equation:

$$L = \lambda_{\overline{\boldsymbol{v}}} L_{\overline{\boldsymbol{v}}} + \lambda_{\overline{\Psi}} L_{\overline{\Psi}} + \lambda_{\overline{\boldsymbol{\sigma}}} L_{\overline{\boldsymbol{\sigma}}} + \lambda_{\dot{\overline{\Phi}}} P_{\dot{\overline{\Phi}}} \tag{10}$$

Here, the terms $\lambda_{\overline{\boldsymbol{v}}}$, $\lambda_{\overline{\Psi}}$, $\lambda_{\overline{\boldsymbol{\sigma}}}$, and $\lambda_{\dot{\overline{\Phi}}}$ represent the weights assigned to each

component within the loss or penalty function. While the terms in L are specified as follows:

$$\begin{cases} L_{\overline{\boldsymbol{v}}} = |\overline{\boldsymbol{v}} - \overline{\boldsymbol{v}}^{\mathrm{ANN}}|, \\ L_{\overline{\Psi}} = |\overline{\Psi} - \overline{\Psi}^{\mathrm{ANN}}|, \\ L_{\overline{\boldsymbol{\sigma}}} = |\overline{\boldsymbol{\sigma}} - \dfrac{\partial \overline{\Psi}^{\mathrm{ANN}}}{\partial \overline{\boldsymbol{\varepsilon}}}|. \end{cases} \tag{11}$$

where $\overline{\boldsymbol{v}}$, $\overline{\Psi}$, and $\overline{\boldsymbol{\sigma}}$ represent the reference values for the quantities of interest, the Helmholtz free energy, and the macroscopic stress, respectively. On the other hand, $\overline{\boldsymbol{v}}^{\mathrm{ANN}}$ and $\overline{\Psi}^{\mathrm{ANN}}$ correspond to the predicted values. The concept of a penalty function $P_{\dot{\overline{\Phi}}}$ is defined in Equation 12. This function is designed to be null when dissipation is positive and to take the absolute value of dissipation when it is negative. Its purpose is to contribute to the loss function L in situations where the dissipation assumes non-physical values, thereby enforcing the MuTINN predictions to be thermodynamically consistent. Mathematically, this penalty function is expressed as follows:

$$P_{\dot{\overline{\Phi}}} = \begin{cases} 0 \quad \text{if} \quad -\dfrac{\partial \overline{\Psi}^{\mathrm{ANN}}}{\partial \overline{\boldsymbol{v}}^{\mathrm{ANN}}} \cdot \dfrac{\Delta \overline{\boldsymbol{v}}^{\mathrm{ANN}}}{\Delta t} \geq 0, \\ \left| -\dfrac{\partial \overline{\Psi}^{\mathrm{ANN}}}{\partial \overline{\boldsymbol{v}}^{\mathrm{ANN}}} \cdot \dfrac{\Delta \overline{\boldsymbol{v}}^{\mathrm{ANN}}}{\Delta t} \right| \quad \text{otherwise} \end{cases} \tag{12}$$

4. Data Generation, Results and Discussion at RVE scale

4.1. Data Generation (Sampling)

The local constitutive models outlined in Section 2 are employed to create a dataset for training, evaluating and testing the MuTINN model. This dataset is generated by simulating the unit cell's response under random in-plane loading conditions using finite element computations. It is important

to note that these constitutive models are initially calibrated for tensile loading and may not be perfectly suited for compression loading scenarios. To comprehensively exclude potential compression effects, we conducted simulations using a stress control approach. Within this framework, we controlled both longitudinal and transverse stress levels, keeping them within the range of 0 to 400 MPa (see Figures 5a and 5d), while allowing shear stress to fluctuate between -50 and 50 MPa (see Figure 5b). These specific stress ranges are thoughtfully chosen to align with our study's requirements.

In each finite element simulation, we computed the quantities of interest denoted as $\overline{v}_k$, with k ranging from 1 to 10. These values are determined by averaging specific ISVs defined at the microscale, within three distinct domains: the matrix domain $\mathfrak{B}_0$, the weft yarns domain $\mathfrak{B}_1$, and the warp yarns domain $\mathfrak{B}_2$, as described in Equations 7, 8, and 9. Additionally, we calculated the Helmholtz free energy $\overline{\Psi}$ over the whole domain using the Equation 4c and the macroscopic strain components $\overline{\boldsymbol{\varepsilon}}^{n+1}$ using the Equation 4b and as seen in Figure 6. These computed quantities are then stored as input variables ($\Delta\overline{\boldsymbol{\varepsilon}}^{n+1}$, $\overline{\boldsymbol{\varepsilon}}^{n}$, $\overline{\boldsymbol{v}}^{n}$) and output variables ($\Delta\overline{\boldsymbol{v}}^{n+1}$, $\overline{\boldsymbol{\Psi}}^{n+1}$, $\overline{\boldsymbol{\sigma}}^{n+1}$) for further analysis and utilization in the MuTINN model.

In this study, we employed a dataset comprising 1200 loading paths including training, validation, and test subsets. Each of these loading paths consisted of 10 discrete steps. These steps involved the application of random stress increments in the longitudinal, transverse, and shear directions, as depicted in Figure 5, which illustrates all the loading paths used for training. Initially, these steps exhibited a narrow range of stress increments, but as the number of steps progressed, this range gradually expanded, highlighting

the apparent reduction in stiffness due to damage and an increase in inelastic strain at the macroscopic scale. To achieve finer granularity, we subdivided each of these steps into 20 increments. Consequently, each loading test generated 200 data points, resulting in a total of 240,000 data points for the entire dataset. This dataset is subsequently divided into three distinct subsets: a training set (60%), a validation set (20%), and a test set (20%). However, in our effort to enhance the model's performance, particularly in Online phase, we introduced random uni-axial loading paths into our sampling approach, exemplified by loading paths 3 and 4, which are visually represented in Figure 5 for applied stress components and Figure 6 for the resulting strain components. In the specific case of loading path 3, it is noteworthy that the transverse and shear stress ($\overline{\sigma}_{22}$ and $\overline{\sigma}_{12}$) exhibited changes, while the longitudinal stress $\overline{\sigma}_{11}$ remained at 0 MPa. Conversely, in loading path 4, only the longitudinal stress ($\overline{\sigma}_{11}$) exhibited variation, while the other stress components maintaining a value of zero.

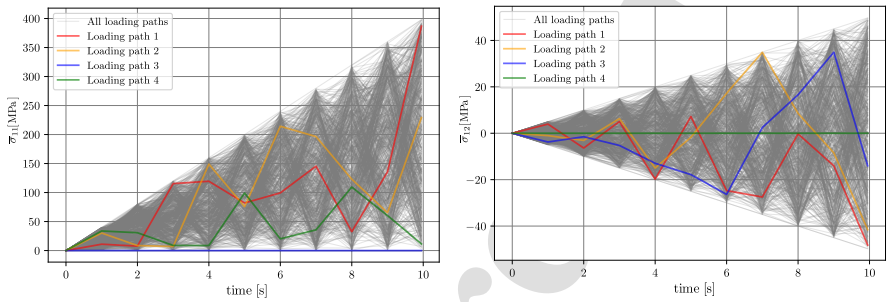

(a) Macroscopic longitudinal stress $\overline{\sigma}_{11}(t)$ (b) Macroscopic shear stress $\overline{\sigma}_{12}(t)$

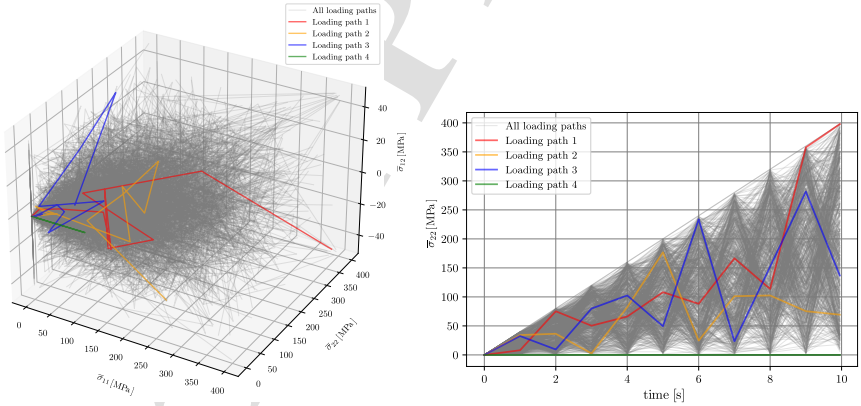

(c) Macroscopic stress ($\overline{\sigma}_{11}$, $\overline{\sigma}_{22}$, $\overline{\sigma}_{12}$) (d) Macroscopic transverse stress $\overline{\sigma}_{22}(t)$

Figure 5: Random loading paths used for training: Macroscopic Stress ($\overline{\sigma}_{11}$, $\overline{\sigma}_{22}$, and $\overline{\sigma}_{12}$).

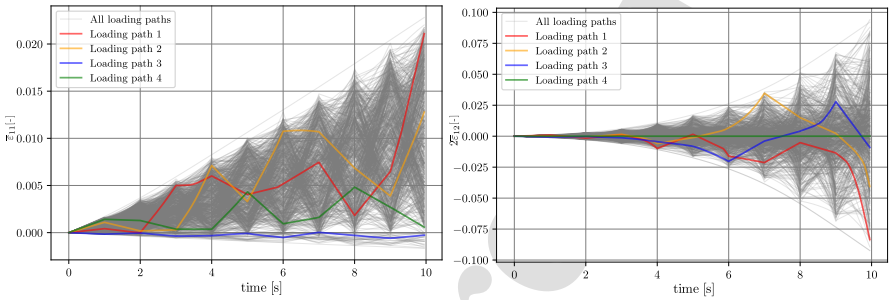

(a) Macroscopic longitudinal strain $\overline{\varepsilon}_{11}(t)$ (b) Macroscopic shear strain $2\overline{\varepsilon}_{12}(t)$

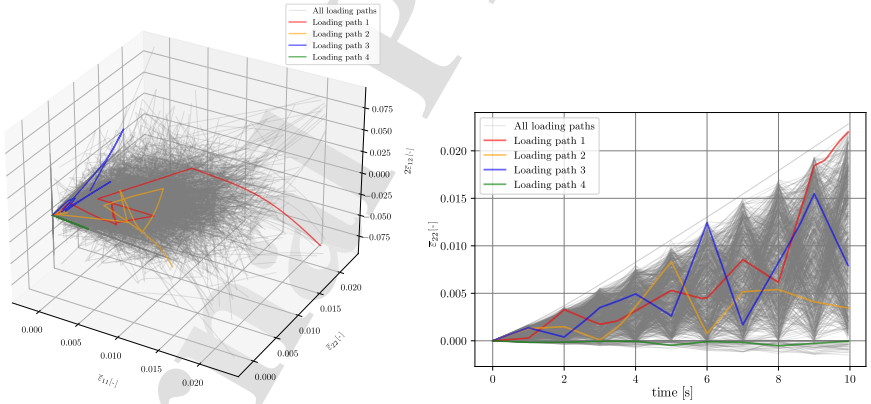

(c) Macroscopic strains ($\overline{\varepsilon}_{11}$, $\overline{\varepsilon}_{22}$, $2\overline{\varepsilon}_{12}$) (d) Macroscopic transverse strain $\overline{\varepsilon}_{22}(t)$

Figure 6: Random loading paths used for training: Macroscopic Strain ($\overline{\varepsilon}_{11}$, $\overline{\varepsilon}_{22}$, and $2\overline{\varepsilon}_{12}$).

4.2. Offline Training and Validation

Before processing for training stage, the dataset, including both input and output sets, underwent normalization to a range of -1 to 1. Subsequently, the MuTINN model was constructed using the open-source neural network computing framework TensorFlow, employing two interconnected artificial neural networks ($ANN_{evolution}$ and ANN_{state}). As summarized in Table 5, each of these neural networks features two hidden layers, with 64 neurons in each layer. The initial network employs the Leaky Rectified Linear Unit activation function (Leaky ReLU) within its hidden layers, while the second network utilizes the Exponential Linear Unit (ELU) as its activation function.

Table 5: MuTINN hyperparameters: The number of layers, number of neurons and the activation function types.

			MuTINN Hyperparameters		
		Inputs Layer	Hidden Layer 1	Hidden Layer 2	Output Layer
$\mathbf{ANN}_{evolution}$	Number of Neurons	16	64	64	10
	Activation function	-	leaky ReLU	leaky ReLU	Linear
$\mathbf{ANN}_{state}$	Number of Neurons	13	64	64	1
	Activation function	-	ELU	ELU	Linear

The model was trained using the Adam algorithm (Kingma and Ba, 2014) with a batch size of 32 and a learning rate set at 10^{-4} -a hyperparameter that governs the rate at which the model's parameters are updated. This learning rate was thoughtfully selected to maintain a delicate equilibrium, preventing convergence issues caused by excessively large values while avoiding extended iteration times associated with excessively small values. Furthermore, Mean

Absolute Error (MAE) is employed to assess the accuracy of predictions made by each ANN. Figure 7 illustrates the progression of MAE across 1500 epochs for both the training and validation datasets for the loss functions $L_{\overline{\boldsymbol{v}}}$, $L_{\overline{\Psi}}$, and $L_{\overline{\boldsymbol{\sigma}}}$. Investigating the results, one can notice that the error rates for both the training and validation sets closely align, indicating that the model was successfully trained, while the issues related to both underfitting and overfitting were restricted. It is worth emphasizing that achieving high accuracy in the predicted quantities of interest is paramount, as these serve as inputs to $\text{ANN}_{\text{state}}$ for the current increment and $\text{ANN}_{\text{evolution}}$ for the subsequent increment. Ensuring precision in $\overline{\boldsymbol{v}}$ is critical to prevent the accumulation of errors that might potentially affect the accuracy of free energy and stress predictions.

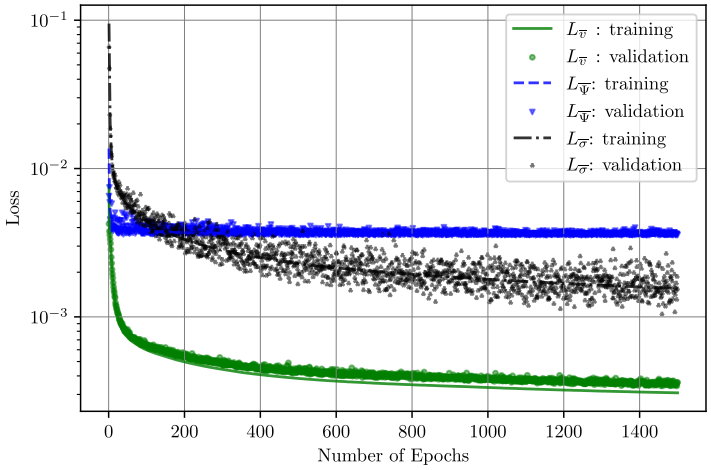

Figure 7: Training and validation of MuTINN model: Variation of loss functions ($L_{\overline{v}}$, $L_{\overline{\Psi}}$ and $L_{\overline{\sigma}}$) with respect to number of epochs.

4.3. Online Testing on unseen loading paths

Once the MuTINN model has completed its training, it is employed in a recall mode (Online phase) to generate predictions for loading paths that are randomly generated and absolutely not included in the training dataset. In the following section, we will illustrate two specific instances of loading scenarios in Figures 8 and 9. These examples aim at providing a concise overview of MuTINN's performance in predicting the macroscopic response of woven composites under complex loading conditions. Each of these Figures is composed of seven subfigures. In the top row, three subfigures depict the randomly applied in-plane macroscopic strains ($\overline{\varepsilon}_{11}$, $\overline{\varepsilon}_{22}$, $2\overline{\varepsilon}_{12}$). Moving to the center, a subfigure visually presents the predicted macroscopic Helmholtz free energy ($\overline{\Psi}$) by MuTINN, along with a comparative analysis against finite element (FE) results. Finally, in the bottom, three subfigures provide a detailed comparison between MuTINN's predictions and the FE simulations based on periodic homogenization, specifically for the macroscopic stresses ($\overline{\sigma}_{11}$, $\overline{\sigma}_{22}$, $\overline{\sigma}_{12}$). As shown in the provided Figures, it is evident that the MuTINN model consistently demonstrates exceptional performance, highlighting its remarkable ability to provide highly accurate predictions for both macroscopic Helmholtz free energy and stresses. However, it is worth pointing out that the strain increment values can affect the overall results particularly for the macroscopic shear response. To limit this effect when applying MuTINN model, in recall mode for a new loading path, it is recommended to employ strain increments within the designated training ranges. Alternatively, these ranges can be expanded during the training phase to increase the overall robustness of the MuTINN model.

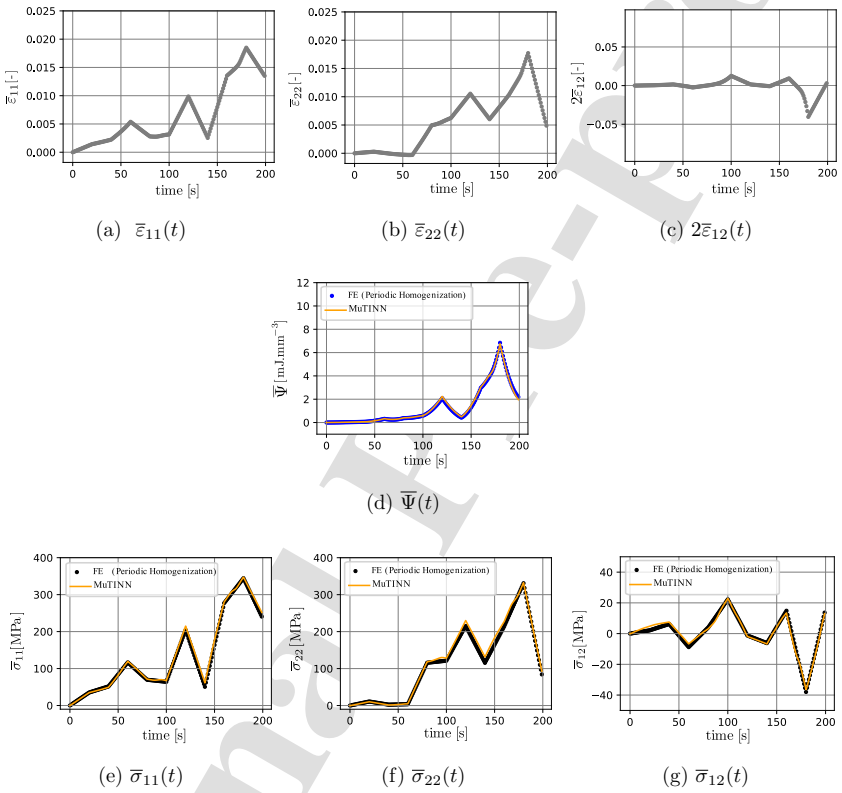

(a) $\overline{\varepsilon}_{11}(t)$ (b) $\overline{\varepsilon}_{22}(t)$ (c) $2\overline{\varepsilon}_{12}(t)$

(d) $\overline{\Psi}(t)$

(e) $\overline{\sigma}_{11}(t)$ (f) $\overline{\sigma}_{22}(t)$ (g) $\overline{\sigma}_{12}(t)$

Figure 8: Comparison of FE-based periodic homogenization and MuTINN approaches for an unseen random loading path N° **1** (Loading path not included in training dataset): (a), (b) and (c) the applied macroscopic strain components $\overline{\varepsilon}_{11}$, $\overline{\varepsilon}_{22}$, and $2\overline{\varepsilon}_{12}$ respectively. (d) the macroscopic Helmholtz free energy ($\overline{\Psi}$). (e), (f), and (g) the macroscopic stress components $\overline{\sigma}_{11}$, $\overline{\sigma}_{22}$, and $\overline{\sigma}_{12}$, respectively.

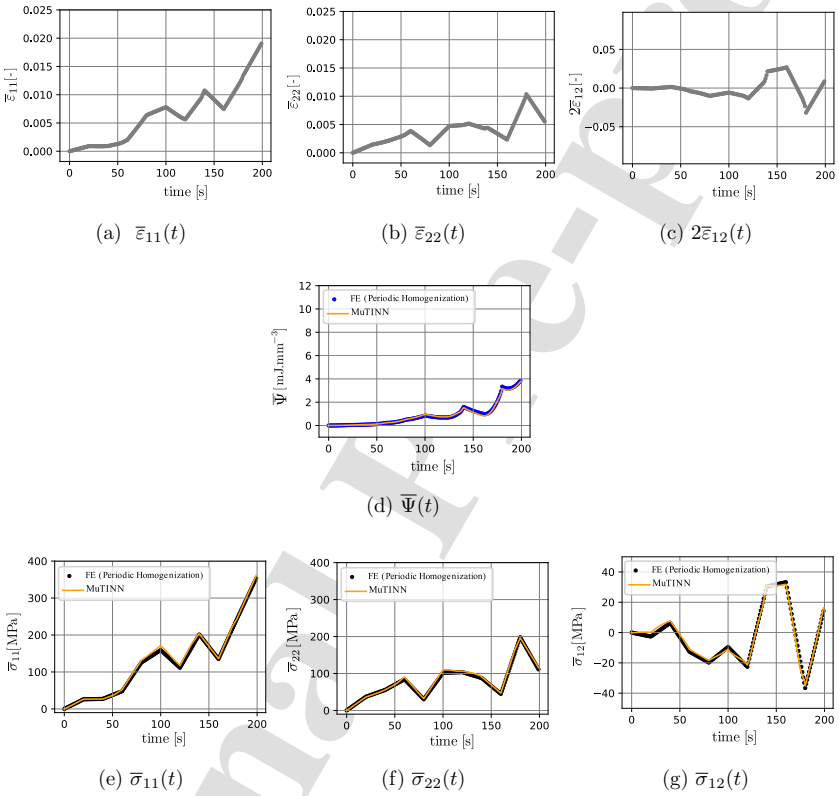

(a) $\overline{\varepsilon}_{11}(t)$ (b) $\overline{\varepsilon}_{22}(t)$ (c) $2\overline{\varepsilon}_{12}(t)$

(d) $\overline{\Psi}(t)$

(e) $\overline{\sigma}_{11}(t)$ (f) $\overline{\sigma}_{22}(t)$ (g) $\overline{\sigma}_{12}(t)$

Figure 9: Comparison of FE-based periodic homogenization and MuTINN approaches for an unseen random loading path N° **2** (Loading path not included in training dataset): (a), (b) and (c) the applied macroscopic strain components $\overline{\varepsilon}_{11}$, $\overline{\varepsilon}_{22}$, and $2\overline{\varepsilon}_{12}$ respectively. (d) the macroscopic Helmholtz free energy ($\overline{\Psi}$). (e), (f), and (g) the macroscopic stress components $\overline{\sigma}_{11}$, $\overline{\sigma}_{22}$, and $\overline{\sigma}_{12}$, respectively.

5. Integration of MuTINN into a FE Code towards Structure Computation

5.1. Numerical Implementation

To seamlessly integrate the MuTINN model into a finite element (FE) code, a Meta-UMAT has been developed using the Fortran programming language. This Meta-UMAT serves as a bridge between the FE commercial software and the MuTINN model as illustrated schematically in Figure 10. In this context, with each incremental step, the Meta-UMAT conducts calculations employing the MuTINN model to ascertain the updated macroscopic stress, denoted as $\overline{\boldsymbol{\sigma}}^{n+1}$, and the corresponding macroscopic tangent modulus, represented as $\overline{\mathbb{C}}_t^{n+1}$, based on the provided macroscopic strain increment $\Delta\overline{\boldsymbol{\varepsilon}}^{n+1}$. However, in order to utilize the trained MuTINN model effectively, the Meta-UMAT necessitates the importation of various essential parameters of the MuTINN model. These parameters include the architecture specifications such as the number of layers, the number of neurons per layer, activation functions, as well as the weights and biases. These critical parameters are retrieved from a previously saved INP file named "Properties.inp".

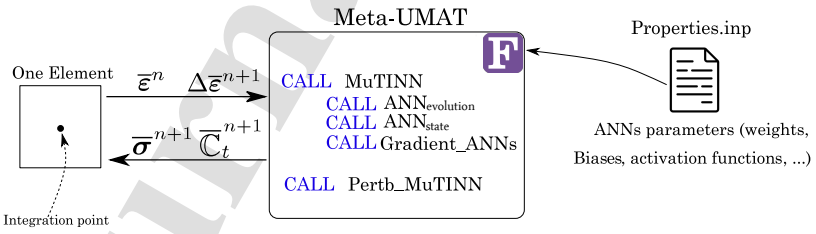

Figure 10: Schematic Implementation of MuTINN into a FE commercial software towards performing structural computations.

As illustrated in Algorithm 1 and Figure 4, MuTINN comprises three distinct functions: $\text{ANN}_{\text{evolution}}$, $\text{ANN}_{\text{state}}$, and Gradient_ANNs. The initial component, $\text{ANN}_{\text{evolution}}$, serves as a feedforward neural network dedicated to describe the evolution law. Its primary purpose is to calculate the updated quantities of interest, represented as $\overline{\boldsymbol{v}}^{n+1}$, for a given strain increment. The second component, $\text{ANN}_{\text{state}}$, corresponds to the state law within the MuTINN framework. This component plays a crucial role in determining the Helmholtz free energy, which is a key factor in the overall behavior of the system. The third and final component of MuTINN is devoted to the computation of the macroscopic stress. This achieves by utilizing automatic differentiation techniques applied to the $\text{ANN}_{\text{state}}$. This integrated approach ensures the accurate calculation of macroscopic stress values within the system.

Algorithm 1 $\overline{\boldsymbol{v}}^{n+1}$, $\overline{\Psi}^{n+1}$, $\overline{\boldsymbol{\sigma}}^{n+1}$=MuTINN($\Delta\overline{\boldsymbol{\varepsilon}}^{n+1}$, $\overline{\boldsymbol{\varepsilon}}^{n}$, $\overline{\boldsymbol{v}}^{n}$)

Require: $\Delta\overline{\boldsymbol{\varepsilon}}^{n+1}$, $\overline{\boldsymbol{\varepsilon}}^{n}$, $\overline{\boldsymbol{v}}^{n}$

$\Delta\overline{\boldsymbol{v}}^{n+1}=\text{ANN}_{\text{evolution}}(\ \Delta\overline{\boldsymbol{\varepsilon}}^{n+1}, \overline{\boldsymbol{\varepsilon}}^{n}, \overline{\boldsymbol{v}}^{n})$ ▷ Feed forward Neural Networks

$\overline{\boldsymbol{v}}^{n+1}=\overline{\boldsymbol{v}}^{n}+\Delta\overline{\boldsymbol{v}}^{n+1}$, $\overline{\boldsymbol{\varepsilon}}^{n+1}=\overline{\boldsymbol{\varepsilon}}^{n}+\Delta\overline{\boldsymbol{\varepsilon}}^{n+1}$

$\overline{\Psi}^{n+1}=\text{ANN}_{\text{state}}(\overline{\boldsymbol{\varepsilon}}^{n+1}, \overline{\boldsymbol{v}}^{n+1})$ ▷ Feed forward Neural Networks

$\overline{\boldsymbol{\sigma}}^{n+1}=$Gradient_ANNs$(\overline{\Psi}^{n+1}, \overline{\boldsymbol{\varepsilon}}^{n+1})$ ▷ Automatic Differentiation

return $\overline{\boldsymbol{v}}^{n+1}$, $\overline{\Psi}^{n+1}$, $\overline{\boldsymbol{\sigma}}^{n+1}$.

The global finite element solver requires the incorporation of the tangent operator $\mathbb{C}_t$, alongside with stress computation. This modulus quantifies the current rate of stress change relative to the total strain variation. For nonlinear behaviors, especially when dealing with a macroscopic problem through

Algorithm 2 $\overline{\mathbb{C}}_t^{n+1}$ =Pertb_MuTINN($\delta\overline{\varepsilon}$, $\Delta\overline{\boldsymbol{\varepsilon}}^{n+1}$, $\overline{\boldsymbol{\varepsilon}}^{n}$, $\overline{\boldsymbol{v}}^{n}$)

Require: $\delta\overline{\varepsilon}$, $\Delta\overline{\boldsymbol{\varepsilon}}^{n+1}$, $\overline{\boldsymbol{\varepsilon}}^{n}$, $\overline{\boldsymbol{v}}^{n}$

$\overline{\boldsymbol{\sigma}}^{n+1}$=MuTINN($\Delta\overline{\boldsymbol{\varepsilon}}^{n+1}$, $\overline{\boldsymbol{\varepsilon}}^{n}$, $\overline{\boldsymbol{v}}^{n}$)

for k=1 to 3 **do**

$\Delta\overline{\boldsymbol{\varepsilon}}_{(k)}^{n+1}$=$\Delta\overline{\boldsymbol{\varepsilon}}^{n+1}$+ $\delta\overline{\varepsilon}\,[\delta_{1k},\,\delta_{2k},\,\delta_{3k}]^{\mathrm{T}}$, $\delta_{ij}=\begin{cases}1 & \text{if } i=j,\\ 0 & \text{else.}\end{cases}$

$\overline{\boldsymbol{\sigma}}_{(k)}^{n+1}$=MuTINN($\Delta\overline{\boldsymbol{\varepsilon}}_{(k)}^{n+1}$, $\overline{\boldsymbol{\varepsilon}}^{n}$, $\overline{\boldsymbol{v}}^{n}$)

$\Delta\overline{\boldsymbol{\sigma}}_{(k)}^{n+1}$=$\overline{\boldsymbol{\sigma}}_{(k)}^{n+1}$-$\overline{\boldsymbol{\sigma}}^{n+1}$

$\overline{\mathbb{C}}_t^{n+1}\cdot[\delta_{1k},\,\delta_{2k},\,\delta_{3k}]^{\mathrm{T}}=\Delta\overline{\boldsymbol{\sigma}}_{(k)}^{n+1}/\delta\overline{\varepsilon}$

end for

return $\overline{\mathbb{C}}_t^{n+1}$

an implicit resolution approach, it becomes essential to calculate the immediate macroscopic tangent operator for each macroscopic increment and at each macroscopic integration point. This particular step plays a critical role in ensuring a fast convergence of the solution within a specified time increment, thereby reducing the number of iterations required to achieve global convergence. For this reason, a perturbation function called Pertb_MuTINN has been developed. As demonstrated in Algorithm 2, this function takes as inputs the current macroscopic strain denoted as $\overline{\boldsymbol{\varepsilon}}^{n}$, the current quantities of interest represented as $\overline{\boldsymbol{v}}^{n}$, the macroscopic strain increment $\Delta\overline{\boldsymbol{\varepsilon}}^{n+1}$, and a constant $\delta\varepsilon$ set to the value of 10^{-4}. It subsequently yields the updated macroscopic tangent modulus $\overline{\mathbb{C}}_t^{n+1}$ as its output. The latter is calculated using the perturbation technique, employing three elementary loading cases:

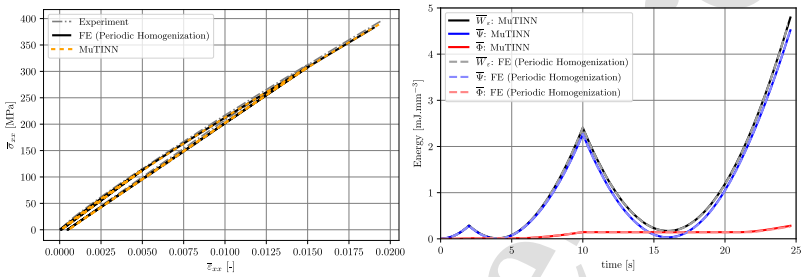

(a) $\overline{\sigma}_{xx}(t)$ vs. $\overline{\varepsilon}_{xx}(t)$ (b) $\overline{W}_\varepsilon(t)$, $\overline{\Psi}(t)$ and $\overline{\Phi}(t)$

Figure 11: Comparative analysis of load-unload testing on woven composite orientations $\pm[0°]_s$: Experiment (Praud et al., 2021) vs. FE-Based Periodic Homogenization vs. MuTINN for stress-strain curve. FE-Based Periodic Homogenization vs. MuTINN for Energies.

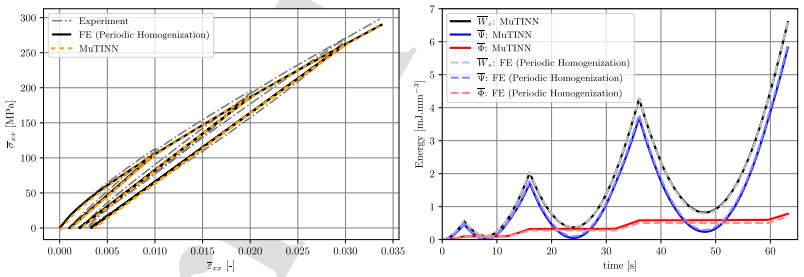

(a) $\overline{\sigma}_{xx}(t)$ vs. $\overline{\varepsilon}_{xx}(t)$ (b) $\overline{W}_\varepsilon(t)$, $\overline{\Psi}(t)$ and $\overline{\Phi}(t)$

Figure 12: Comparative analysis of load-unload testing on woven composite orientations $\pm[30°]_s$: Experiment (Praud et al., 2021) vs. FE-Based Periodic Homogenization vs. MuTINN for stress-strain curve. FE-Based Periodic Homogenization vs. MuTINN for Energies.

$[\delta\varepsilon, 0, 0]^{\mathrm{T}}$, $[0, \delta\varepsilon, 0]^{\mathrm{T}}$, and $[0, 0, \delta\varepsilon]^{\mathrm{T}}$. It is important to note that this modulus may not necessarily exhibit major symmetry.

To validate the framework developed herein, we initiate the process by performing computations at a single macroscopic point, representing one element, which is equivalent to the computations conducted at the Unit Cell scale. To this end, three configurations of woven composite laminates have been selected: $\pm[0°]_{\mathrm{s}}$, $\pm[30°]_{\mathrm{s}}$, and $\pm[45°]_{\mathrm{s}}$. Each of these laminates has undergone load-unload tests, with loading carried out under strain control and unloading under free stress control. Subsequently, we compare the results obtained from experimental tests with those acquired through Finite Element periodic homogenization at the unit cell scale and FE-MuTINN analysis for a single macroscopic point, yielding the following findings. It is worth noting that the response of a multilayered composite is usually simulated

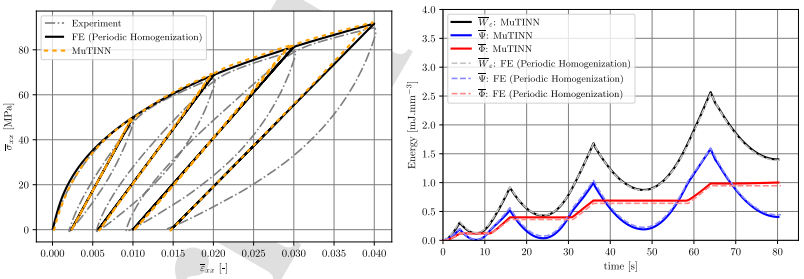

(a) $\overline{\sigma}_{xx}(t)$ vs. $\overline{\varepsilon}_{xx}(t)$ (b) $\overline{W}_\varepsilon(t)$, $\overline{\Psi}(t)$ and $\overline{\Phi}(t)$

Figure 13: Comparative analysis of load-unload testing on woven composite orientations $\pm[45°]_{\mathrm{s}}$: Experiment (Praud et al., 2021) vs. FE-Based Periodic Homogenization vs. MuTINN for stress-strain curve. FE-Based Periodic Homogenization vs. MuTINN for Energies.

through the classical laminate theory, detailed in several books among them: (Öchsner, 2021; Chatzigeorgiou et al., 2022). More straightforwardly, in the case of a symmetric and balanced laminate ($\pm[\theta^\circ]_s$), the uni-axial response can be directly simulated by considering only one single layer oriented at θ, i.e., one single macroscopic material point, retaining vanishing in-plane shear strain in the laminate coordinate system, as explained in (Praud, 2018). This methodology will be employed in the current study for conducting FE-based periodic homogenization on the unit cell and MuTINN predictions on a single element (a macroscopic material point).

Figures 11a, 12a, and 13a depict a comparative analysis of stress-strain curves for a symmetrical and balanced woven composite laminate subjected to a load-unload test. This comparison involves examining experimental data previously obtained in (Praud et al., 2021) and comparing it with the outcomes generated through the FE-based periodic homogenization and MuTINN approaches for laminate woven composites oriented at angles of $\pm[0^\circ]_s$, $\pm[30^\circ]_s$, and $\pm[45^\circ]_s$, respectively. Upon careful examination of these Figures, it becomes evident that there is a high degree of agreement between the predictions of stress-strain curves made by the FE and MuTINN methods across the various orientations studied, as well as when compared to the experimental results. Furthermore, the MuTINN model effectively captures the reduction in stiffness due to the presence of damage mechanisms associated with the initiation, growth, and coalescence of micro-cracks within the yarns. This phenomenon is particularly noticeable during the unloading stage, especially for the laminate orientation of $\pm[45^\circ]_s$.

Figures 11b, 12b, and 13b present a comprehensive analysis of various

energy metrics in the context of a load-unload test applied to a symmetrical and balanced woven composite laminate. These metrics include strain energy ($\overline{W}_{\boldsymbol{\varepsilon}}$ as defined in Equation 13), Helmholtz free energy ($\overline{\Psi}$), and dissipation energy ($\overline{\Phi}$ as defined in Equation 14). This comparative examination employs two distinct methodologies: Finite Element (FE)-based periodic homogenization and MuTINN. The focus of this analysis centers on laminate composites denoted as $\pm[0°]_{\mathrm{s}}$, $\pm[30°]_{\mathrm{s}}$, and $\pm[45°]_{\mathrm{s}}$ orientations. These Figures reveal a strong correlation between the energy values predicted by the MuTINN model and the reference values obtained through full-field periodic homogenization for the different orientations. Consequently, these findings provide compelling evidence for the thermodynamic consistency of the predictions generated by the MuTINN model.

$$\overline{W}_{\varepsilon} = \int_{\overline{\boldsymbol{\varepsilon}}} \overline{\boldsymbol{\sigma}} \cdot \mathrm{d}\overline{\boldsymbol{\varepsilon}} = \int_{\overline{\boldsymbol{\varepsilon}}} \frac{\partial \overline{\Psi}}{\partial \overline{\boldsymbol{\varepsilon}}} \cdot \mathrm{d}\overline{\boldsymbol{\varepsilon}}, \tag{13}$$

$$\overline{\Phi} = \int_{\overline{\boldsymbol{v}}} -\frac{\partial \overline{\Psi}}{\partial \overline{\boldsymbol{v}}} \cdot \mathrm{d}\overline{\boldsymbol{v}}. \tag{14}$$

After conducting the calculations, we have observed a significant reduction in computational time when employing the FE-MuTINN, as outlined in Table 6. It is evident that the use of FE-MuTINN results in computations taking only few seconds, whereas traditional FE-based periodic homogenization typically demands several minutes for the same time intervals. This feature renders the FE-MuTINN approach a suitable choice for handling large-scale composite structures.

Table 6: Comparative analysis of CPU time: FE-Based Periodic Homogenization at the UC scale vs. FE-MuTINN at a macroscopic point for load-unload testing of three different orientations.

		Orientation		
	Approach	$[\pm 0°]_s$	$[\pm 30°]_s$	$[\pm 45°]_s$
CPU time	FE (Periodic homogenization)	9min 31s	27min 53 s	35min 35s
	FE-MuTINN	3s	21s	32s

5.2. Application of FE-MuTINN for composite structure analysis

After establishing a robust framework that integrates MuTINN with a commercial finite element computation software and successfully training the MuTINN model, the next crucial phase involves harnessing its capabilities in practical applications within the field of composite engineering structures. As shown in Figure 14, in contrast to FE^2, which utilized FE analysis at both the structural and unit cell scales, FE-MuTINN, as its name suggests, allows for the utilization of FE at the structural scale while deploying MuTINN at each integration point. This innovative approach represents a significant departure from previous methodologies, offering distinct advantages and novel insights into composite engineering.

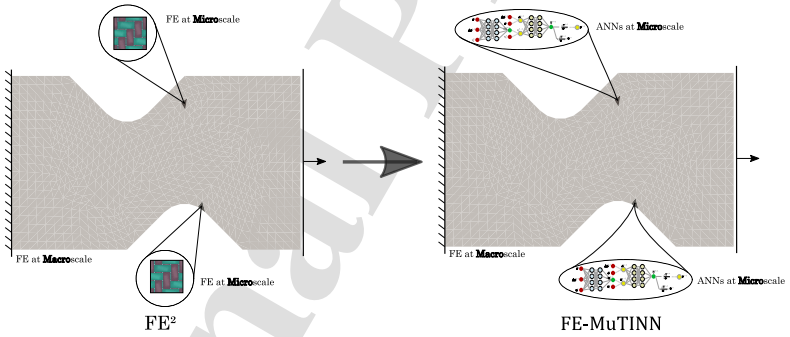

Figure 14: Schematic representation of FE^2 and FE-MuTINN approaches.

In this research, the Open Hole specimen is employed to conduct the composite structure analysis. This selection is based on the availability of experimental data from prior research (Tikarrouchine et al., 2021), which closely matches the exact structural dimensions and employs the same re-

inforcement and matrix materials as those used in our investigation. The examined structure has specific measurements, with a length of 120.0 mm, a width of 60.0 mm, and a thickness of 1.0 mm. Notably, it includes a cen-

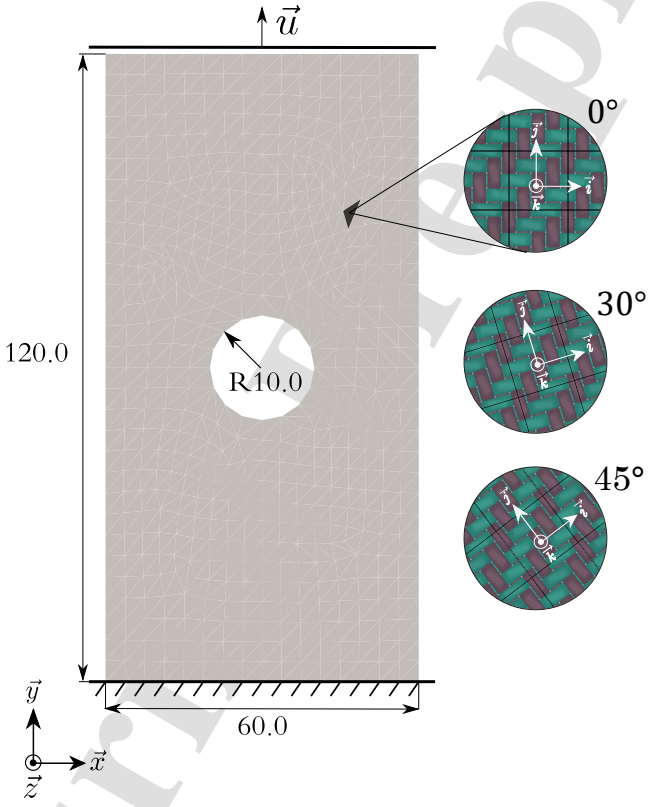

Figure 15: Displacement control tension on Open-Hole woven composite structure: Dimension, Loading and Boundary Conditions ($\vec{u} = (1.0, 0)$ mm for 0°, $\vec{u} = (2.5, 0)$ mm for 30° and $\vec{u} = (3.5, 0)$ mm for 45°).

trally located hole with a 10.0 mm radius, as illustrated in Figure 15. Ideally, to be in line with scale separation assumption, the characteristic size of the structure should be sufficiently higher than the unit cell characteristic dimensions. However, in the current structure, it appears that the characteristic size of the structure is approximately four times larger than the unit cell size, specifically 15×15 mm^2. Even though this ratio does not totally guarantee the scale separation, the comparison between the experimental results and FE predictions demonstrate that this ratio could be sufficient for this type of structure. Furthermore, due to the experimental setup limitations in terms of load-cell capacity and tension grips size, it is not easy to perform tests for large scale structure that totally ensure the scale separation.

As illustrated in the Figure 15, this structure is subject to specific boundary conditions and loading. Consequently, the lower face of the structure is firmly clamped within the plane. Conversely, on the upper face, we impose constraints such that displacements along the x-axis remain at zero, while a non-zero displacement along the y-axis is applied, denoted as $\vec{u} = (u_{xx} = 0, u_{yy} \neq 0)$. Moreover, in this analysis, we have investigated the composite structure through three distinct configurations, each defined by a single layer reinforced with woven fabric and orientated at angles 0°, 30°, and 45° with respect to the principal axes ($\vec{x}$, $\vec{y}$, $\vec{z}$). For each orientation, we apply distinct displacements: $u_{yy} = 1.0$ mm for the 0° configuration, $u_{yy} = 2.5$ mm for the 30° configuration, and $u_{yy} = 3.5$ mm for the 45° configuration. Furthermore, the structure is discretized using a total of 514 plane stress elements, comprising both three-node plane stress elements (CPS3) and four-node plane stress elements (CPS4). It is imperative to emphasize that we choose to evaluate

the feasibility and the predictions capabilities of MuTINN on thin composite structure computations assuming the plane stress assumption. Nevertheless, the MuTINN model can also be extended to 3D problems in a straightforward manner. However, achieving this would necessitate much more information to train MuTINN, specifically all the macroscopic stress and strain components ($\overline{\sigma}_{11}$, $\overline{\sigma}_{22}$, $\overline{\sigma}_{33}$, $\overline{\sigma}_{12}$, $\overline{\sigma}_{13}$, $\overline{\sigma}_{23}$) and ($\overline{\varepsilon}_{11}$, $\overline{\varepsilon}_{22}$, $\overline{\varepsilon}_{33}$, $2\overline{\varepsilon}_{12}$, $2\overline{\varepsilon}_{13}$, $2\overline{\varepsilon}_{23}$), and possibly more internal quantities to properly described the macroscopic state under 3D loading paths.

Building upon the previous section's discussion regarding the implementation of MuTINN into the FE code, our implementation of FE-MuTINN has yielded notable success in carrying out simulations for diverse structural configurations within mere minutes of CPU time. This is vividly exemplified in the data presented in Table 7. This stands in stark contrast to the significantly higher computational costs that would have been incurred if we had opted for FE^2 analysis, which would have demanded several hours to even days of computation. The outcomes produced through FE-MuTINN computations have been graphically represented as force-displacement curves in Figure 16. These findings align closely with the experimental data detailed in (Tikarrouchine et al., 2021). In the experimental setup, the Open-Hole specimens underwent a conditioning process within a controlled climatic chamber. Throughout this procedure, the specimens are conditioned at an atmosphere characterized by a relative humidity of 50% at a temperature of 65°C. This conditioning process is maintained until the water concentration within the specimens reached a relatively uniform level of 2.8%. Subsequently, two distinct sets of tests are conducted. The first set involved the specimen

reinforced with woven fabric composite oriented at 0°, subjected to monotonic tensile tests at two distinct displacement rates: 0.024 and 0.24 mm.s^{-1}. These tests continued until the point of macroscopic fracture is reached. In contrast, the second set of tests focused on the specimen reinforced with 45 degrees woven fabric, employing displacement rates of 0.033 and 0.33 mm.s^{-1} and continuing until macroscopic fracture is observed. In general, the global behavior of the composite structures exhibits a non-linear response. This response can be attributed to either the rheology of the PA66 matrix and/or the degradation in the yarns caused by the presence of micro-cracks, as elaborated in the forthcoming Figures.

Table 7: Computational Efficiency: CPU Time for woven composite structure analysis using FE-MuTINN method.

		Number of Elements	Orientation		
		CPS3 and CPS4	0°	30°	45°
CPU time	Open-hole structure	514	1min 44s	1min 46s	1min 46s

It is imperative to emphasize that the thermoplastic matrix typically displays time-dependent behavior. However, the existing constitutive model utilized to train our current model is time-independent. Consequently, it fails to account for the influence of displacement or strain rate on the composite's overall response, thus elucidating the slight disparity between experimental and numerical results. This prompts us to focus our upcoming research primarily on the integration of viscoelastic and viscoplastic characteristics into our model.

To provide a more thorough insight into the results, we have illustrated

the spatial distribution of three key parameters of interest: $\overline{v}_1$, $\overline{v}_5$, and $\overline{v}_8$, along with the macroscopic strain fields $\overline{\varepsilon}_{11}$, $\overline{\varepsilon}_{22}$, and $2\overline{\varepsilon}_{12}$. These variables were examined across three different fabric orientations as shown in the Figures 17, 18, and 19 for ($\overline{v}_1$, $\overline{v}_5$, and $\overline{v}_8$) and in Figures 20, 21, and 22 for ($\overline{\varepsilon}_{11}$, $\overline{\varepsilon}_{22}$, and $2\overline{\varepsilon}_{12}$). These configurations effectively showcase all the fields at various displacements: specifically, 1 mm for 0 degrees, 2 mm for 30 degrees, and 3 mm for 45 degrees. As previously discussed, it is important to note that

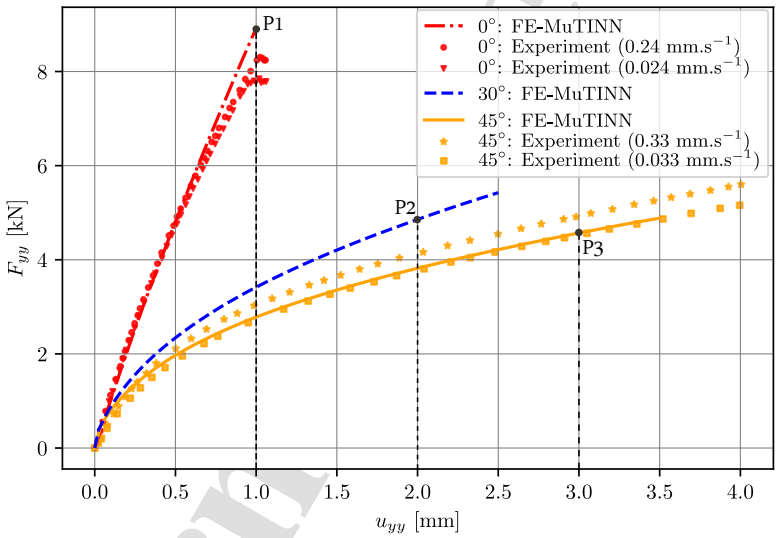

Figure 16: Comparative analysis of Force-Displacement curves for Open-Hole woven composite structures: FE-MuTINN simulations with variable woven fabric orientations (0°, 30°, and 45°) under displacement control along the $\vec{x}$ axis, and their correlation with experimental data from (Tikarrouchine et al., 2021) at different displacement rates: $\dot{u}_{yy}$=0.24 mm.s^{-1} and $\dot{u}_{yy}$=0.024 mm.s^{-1} for 0°. $\dot{u}_{yy}$=0.33 mm.s^{-1} and $\dot{u}_{yy}$=0.033 mm.s^{-1} for 45°.

quantities of interest ($\overline{v}_1$, $\overline{v}_5$, and $\overline{v}_8$) are directly linked to critical aspects of the material's behavior, representing the average accumulated plastic strain in the matrix, the average micro-crack density in the weft, and the warp yarns, respectively.

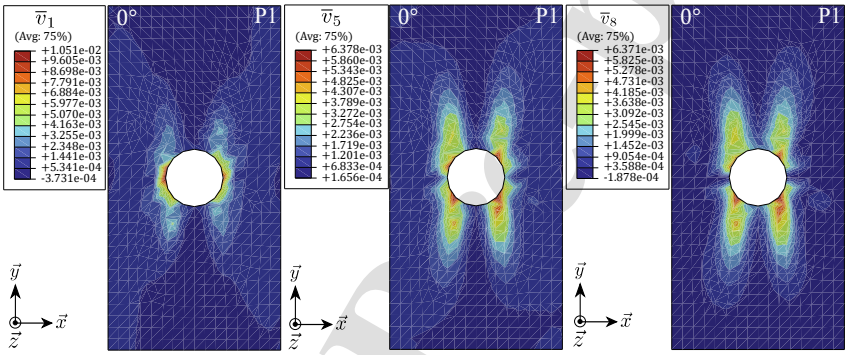

(a) $\overline{v}_1$ at u_{yy}=1.00 mm for 0°. (b) $\overline{v}_5$ at u_{yy}=1.00 mm for 0°. (c) $\overline{v}_8$ at u_{yy}=1.00 mm for 0°.

Figure 17: FE-MuTINN results for an Open-Hole structure reinforced with a 0° oriented woven composite subjected to a displacement of u_{yy}=1.00 mm. (a) $\overline{v}_1$: Average accumulated plastic strain in the matrix. (b) $\overline{v}_5$: Average micro-crack density in the weft yarns. (c) $\overline{v}_8$: Average micro-crack density in the warp yarns.

Figures 17, 18, and 19 offer a detailed local perspective of the area surrounding the hole, providing a comprehensive insight into the primary phenomena observed in the tested specimens. Furthermore, the Figures 20, 21, and 22 provide qualitative observations of macroscopic strain fields, validating the DIC strain localization maps obtained in (Tikarrouchine et al., 2021). These results stem from the localized plastic deformation within the matrix and micro-damage within the yarns, such as localized de-bonding or

micro-cracking, which ultimately leads to fiber breakage. In general, when considering the composite structure with a 45° woven orientation, the simulation demonstrates a distinctive pattern. It unveils an inhomogeneous and symmetric distribution of $\overline{v}_1$, $\overline{v}_5$, and $\overline{v}_8$. This distribution gives rise to banded regions that align at a 45° angle relative to the applied load direction. Conversely, when examining the composite structure with a 30° woven orientation, a different scenario emerges. The simulation reveals an inhomogeneous and asymmetric distribution of the same variables, $\overline{v}_1$, $\overline{v}_5$, and $\overline{v}_8$. These variables form banded regions that are now aligned at a 30° angle relative to the applied load direction.

It is worth noting that the appearance of low negative values in the color-

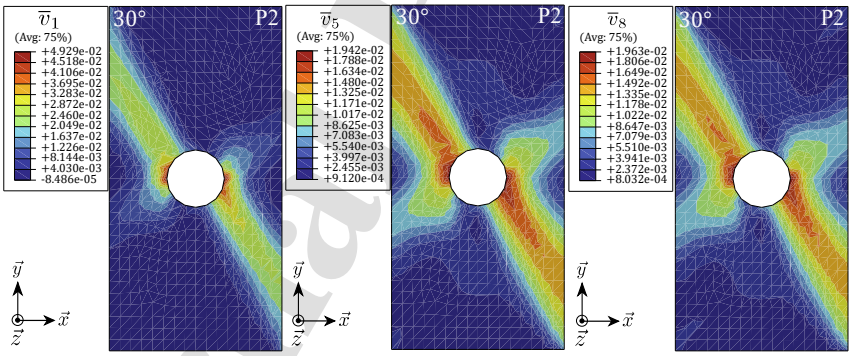

(a) $\overline{v}_1$ at u_{yy}=2.00 mm for 30°.(b) $\overline{v}_5$ at u_{yy}=2.00 mm for 30°.(c) $\overline{v}_8$ at u_{yy}=2.00 mm for 30°.

Figure 18: FE-MuTINN results for an Open-Hole structure reinforced with a 30° oriented woven composite subjected to a displacement of u_{yy}=2.00 mm. (a) $\overline{v}_1$: Average accumulated plastic strain in the matrix. (b) $\overline{v}_5$: Average micro-crack density in the weft yarns. (c) $\overline{v}_8$: Average micro-crack density in the warp yarns.

bar label of certain results can be traced back to specific structural elements undergoing compression loads, especially near the boundary. This disparity arises due to the fact that the MuTINN model has been trained exclusively for tensile loading, as mentioned earlier. Therefore, it is imperative to incorporate compression loading pathways into the training datasets in our forthcoming work.

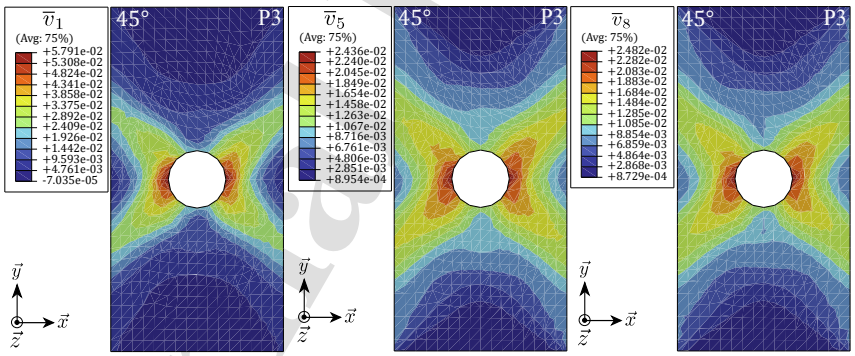

(a) $\overline{v}_1$ at u_{yy}=3.00 mm for 45°.(b) $\overline{v}_5$ at u_{yy}=3.00 mm for 45°.(c) $\overline{v}_8$ at u_{yy}=3.00 mm for 45°.

Figure 19: FE-MuTINN results for an Open-Hole structure reinforced with a 45° oriented woven composite subjected to a displacement of u_{yy}=3.00 mm. (a) $\overline{v}_1$: Average accumulated plastic strain in the matrix. (b) $\overline{v}_5$: Average micro-crack density in the weft yarns. (c) $\overline{v}_8$: Average micro-crack density in the warp yarns.

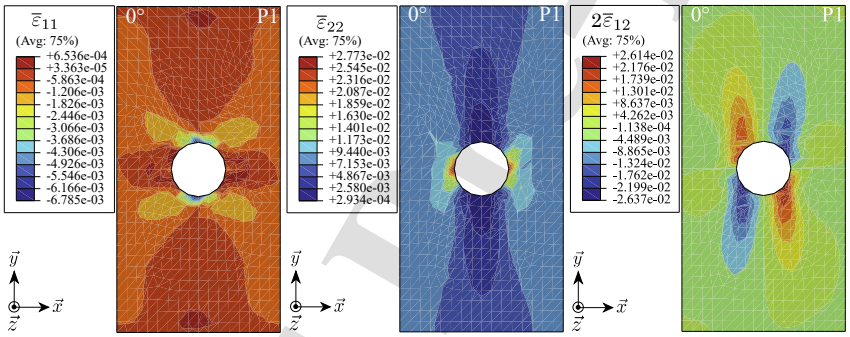

(a) $\overline{\varepsilon}_{11}$ at u_{yy}=1 mm for 0°. (b) $\overline{\varepsilon}_{22}$ at u_{yy}=1 mm for 0°. (c) $2\overline{\varepsilon}_{12}$ at u_{yy}=1 mm for 0°.

Figure 20: FE×MuTINN results for an Open-Hole structure reinforced with a 0° oriented woven composite subjected to a displacement of u_{yy}=1.00 mm. (a) $\overline{\varepsilon}_{11}$: Macroscopic transverse strain. (b) $\overline{\varepsilon}_{22}$: Macroscopic longitudinal strain. (c) $2\overline{\varepsilon}_{12}$: Macroscopic shear strain.

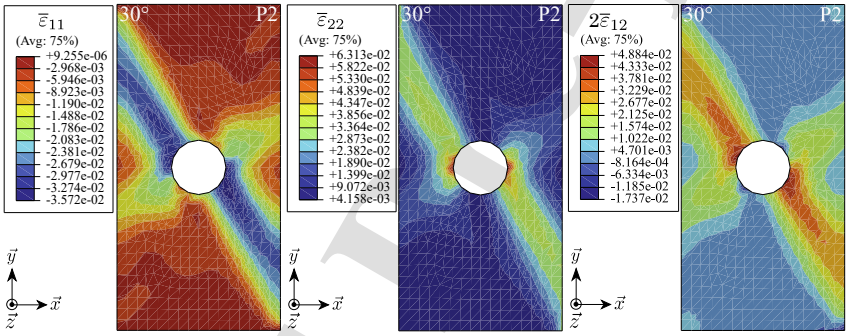

(a) $\bar{\varepsilon}_{11}$ at u_{yy}=2 mm for 30°. (b) $\bar{\varepsilon}_{22}$ at u_{yy}=2 mm for 30°. (c) $2\bar{\varepsilon}_{12}$ at u_{yy}=2 mm for 30°.

Figure 21: FE×MuTINN results for an Open-Hole structure reinforced with a 30° oriented woven composite subjected to a displacement of u_{yy}=2.00 mm. (a) $\bar{\varepsilon}_{11}$: Macroscopic transverse strain. (b) $\bar{\varepsilon}_{22}$: Macroscopic longitudinal strain. (c) $2\bar{\varepsilon}_{12}$: Macroscopic shear strain.

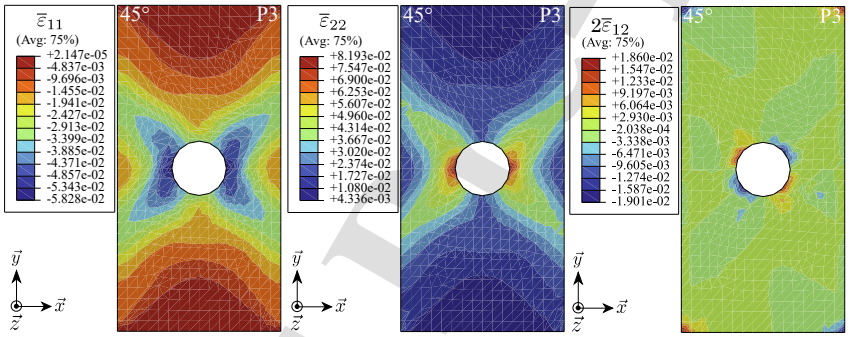

(a) $\bar{\varepsilon}_{11}$ at u_{yy}=3 mm for 45°. (b) $\bar{\varepsilon}_{22}$ at u_{yy}=3 mm for 45°. (c) $2\bar{\varepsilon}_{12}$ at u_{yy}=3 mm for 45°.

Figure 22: FE×MuTINN results for an Open-Hole structure reinforced with a 45° oriented woven composite subjected to a displacement of u_{yy}=3.00 mm. (a) $\bar{\varepsilon}_{11}$: Macroscopic transverse strain. (b) $\bar{\varepsilon}_{22}$: Macroscopic longitudinal strain. (c) $2\bar{\varepsilon}_{12}$: Macroscopic shear strain.

6. Conclusions and Perspectives

Due to the complex nature of woven composite microstructures and their nonlinear behavior, predicting their response using finite element-based multiscale analysis has proven arduous and time-consuming. To tackle these challenges, this work presents an innovative approach that harnesses Artificial Neural Networks (ANNs) alongside fundamental thermodynamic principles, guided by crucial physical parameters. This approach serves as an effective surrogate model, streamlining the process of conducting multiscale analyses. In essence, our research yields a set of vital insights that can be concisely summarized as follows:

- **MuTINN's Incorporation of Physical Quantities:** MuTINN adeptly integrates physical parameters as ISVs at the macroscale. This unique feature allows it to accurately capture the history-dependent behavior of heterogeneous materials under various loading conditions. Furthermore, these quantities offer a valuable physical interpretation by tracking metrics such as damage density and accumulated plastic strain.
- **Thermodynamic Consistency for Reliable Predictions:** MuTINN's adherence to thermodynamic principles significantly enhances the reliability of its predictions, especially when dealing with random loading paths. This attribute renders it an invaluable tool for a wide array of engineering applications.
- **Reduced Training Data Requirements:** The absence of the need to learn the hidden laws of the thermodynamic principle reduces the data required for training, making MuTINN exceptionally effective and

frugal for applications in the field of material science, especially when generating vast amounts of data is challenging.

- **Successful Integration into a Commercial Finite Element Software:** MuTINN model has been successfully implemented into a commercial finite element software package, ensuring its accessibility and versatility in practical engineering contexts.

- **Accelerating Two-Scale Simulations of Composite Structures:** The integration of MuTINN into a FE code provides the additional advantage of accelerating two-scale concurrent simulations, replacing finite element computations at the RVE scale with a MuTINN-based surrogate model.

When it comes to improving achieved results, especially at the structural scale, it is beneficial to incorporate compression loading paths into the training process. This helps prevent the occurrence of non-physical values for quantities of interest in certain regions of the structure when subjected to complex loading and boundary conditions. Additionally, it would be intriguing to compare a two-scale finite element (FE^2) approach with the FE-MuTINN method in terms of both accuracy and computational time. However, regarding future work, the developed MuTINN model holds promise for effectively handling a wide range of heterogeneous materials with intricate microstructures and complex behaviors, requiring only minor adjustments. Therefore, the next advances in model implementation should involve the integration of rate and temperature-dependent behavior of woven composites, with a particular focus on capturing the viscoelastic-viscoplastic character-

istics of the matrix material. In the near future, further research efforts will focus on incorporating a variety of microstructural parameters into the FE-MuTINN model. The ultimate aim resides in accelerating the robust structural analysis in relation to the optimization of process-induced microstructures.

Acknowledgments

The authors gratefully acknowledge ESI Chair for the support that greatly assisted this research, and the Arts et Métiers High Performance Computing Center Cassiopee made available for conducting the research reported in this paper.

References

Agrawal, A., Choudhary, A., 2016. Perspective: Materials informatics and big data: Realization of the "fourth paradigm" of science in materials science. Apl Materials 4.

Aliabadi, M.F., 2015. Woven composites. volume 6. World Scientific.

Barral, M., Chatzigeorgiou, G., Meraghni, F., Léon, R., 2020. Homogenization using modified mori-tanaka and tfa framework for elastoplastic-viscoelastic-viscoplastic composites: Theory and numerical validation. International Journal of Plasticity 127, 102632.

Castaneda, P.P., 2002. Second-order homogenization estimates for nonlinear composites incorporating field fluctuations: I—theory. Journal of the Mechanics and Physics of Solids 50, 737–757.

Castaneda, P.P., Suquet, P., 1997. Nonlinear composites. Advances in applied mechanics 34, 171–302.

Chaboche, J.L., 1989. Constitutive equations for cyclic plasticity and cyclic viscoplasticity. International journal of plasticity 5, 247–302.

Chaboche, J.L., 2008. A review of some plasticity and viscoplasticity constitutive theories. International journal of plasticity 24, 1642–1693.

Chatzigeorgiou, G., Meraghni, F., 2019. Elastic and inelastic local strain fields in composites with coated fibers or particles: Theory and validation. Mathematics and Mechanics of Solids 24, 2858–2894.

Chatzigeorgiou, G., Meraghni, F., Charalambakis, N., 2022. Multiscale modeling approaches for composites. Elsevier.

Chen, Q., Jia, R., Pang, S., 2021. Deep long short-term memory neural network for accelerated elastoplastic analysis of heterogeneous materials: An integrated data-driven surrogate approach. Composite Structures 264, 113688.

Chinesta, F., Ammar, A., Cueto, E., 2010. Recent advances and new challenges in the use of the proper generalized decomposition for solving multidimensional models. Archives of Computational methods in Engineering 17, 327–350.

Chinesta, F., Cueto, E., 2022. Empowering engineering with data, machine learning and artificial intelligence: a short introductive review. Advanced Modeling and Simulation in Engineering Sciences 9, 21.

Chinesta, F., Ladeveze, P., Cueto, E., 2011. A short review on model order reduction based on proper generalized decomposition. Archives of Computational Methods in Engineering 18, 395–404.

Cueto, E., Chinesta, F., 2023. Thermodynamics of learning physical phenomena. Archives of Computational Methods in Engineering , 1–14.

Danoun, A., Prulière, E., Chemisky, Y., 2022. Thermodynamically consistent recurrent neural networks to predict non linear behaviors of dissipative materials subjected to non-proportional loading paths. Mechanics of Materials 173, 104436.

Dvorak, G., Bahei-El-Din, Y., Wafa, A., 1994a. The modeling of inelastic composite materials with the transformation field analysis. Modelling and Simulation in Materials Science and Engineering 2, 571.

Dvorak, G., Wafa, A., Bahei-El-Din, Y., 1994b. Implementation of the transformation field analysis for inelastic composite materials. Computational mechanics 14, 201–228.

Dvorak, G.J., Benveniste, Y., 1992. On transformation strains and uniform fields in multiphase elastic media. Proceedings of the Royal Society of London. Series A: Mathematical and Physical Sciences 437, 291–310.

Eghbalian, M., Pouragha, M., Wan, R., 2023. A physics-informed deep neural network for surrogate modeling in classical elasto-plasticity. Computers and Geotechnics 159, 105472.

El Fallaki Idrissi, M., Praud, F., Champaney, V., Chinesta, F., Meraghni, F., 2022. Multiparametric modeling of composite materials based on non-intrusive pgd informed by multiscale analyses: Application for real-time stiffness prediction of woven composites. Composite Structures 302, 116228.

El Said, B., 2023. Predicting the non-linear response of composite materials

using deep recurrent convolutional neural networks. International Journal of Solids and Structures 276, 112334.

Eshelby, J., 1956. The continuum theory of lattice defects, in: Solid state physics. Elsevier. volume 3, pp. 79–144.

Feyel, F., Chaboche, J.L., 2000. Fe^2 multiscale approach for modelling the elastoviscoplastic behaviour of long fibre sic/ti composite materials. Computer methods in applied mechanics and engineering 183, 309–330.

Frank, M., Drikakis, D., Charissis, V., 2020. Machine-learning methods for computational science and engineering. Computation 8, 15.

Gajek, S., Schneider, M., Böhlke, T., 2021. An fe–dmn method for the multiscale analysis of short fiber reinforced plastic components. Computer Methods in Applied Mechanics and Engineering 384, 113952.

Gajek, S., Schneider, M., Böhlke, T., 2022. An fe-dmn method for the multiscale analysis of thermomechanical composites. Computational Mechanics 69, 1087–1113.

Ghane, E., Fagerström, M., Mirkhalaf, M., 2023. Recurrent neural networks and transfer learning for elasto-plasticity in woven composites. arXiv preprint arXiv:2311.13434 .

Ghavamian, F., Simone, A., 2019. Accelerating multiscale finite element simulations of history-dependent materials using a recurrent neural network. Computer Methods in Applied Mechanics and Engineering 357, 112594.

Glikson, E., Woolley, A.W., 2020. Human trust in artificial intelligence: Review of empirical research. Academy of Management Annals 14, 627–660.

Ibanez, R., Abisset-Chavanne, E., Aguado, J.V., Gonzalez, D., Cueto, E., Chinesta, F., 2018. A manifold learning approach to data-driven computational elasticity and inelasticity. Archives of Computational Methods in Engineering 25, 47–57.

Jiang, J., Wu, J., Chen, Q., Chatzigeorgiou, G., Meraghni, F., 2023. Physically informed deep homogenization neural network for unidirectional multiphase/multi-inclusion thermoconductive composites. Computer Methods in Applied Mechanics and Engineering 409, 115972.

Karniadakis, G.E., Kevrekidis, I.G., Lu, L., Perdikaris, P., Wang, S., Yang, L., 2021. Physics-informed machine learning. Nature Reviews Physics 3, 422–440.

King, R.D., Roberts, S., 2018. Artificial intelligence and machine learning in science.

Kingma, D.P., Ba, J., 2014. Adam: A method for stochastic optimization. arXiv preprint arXiv:1412.6980 .

Kirchdoerfer, T., Ortiz, M., 2016. Data-driven computational mechanics. Computer Methods in Applied Mechanics and Engineering 304, 81–101.

Liu, X., Tian, S., Tao, F., Yu, W., 2021. A review of artificial neural networks in the constitutive modeling of composite materials. Composites Part B: Engineering 224, 109152.

Liu, Z., Bessa, M., Liu, W.K., 2016. Self-consistent clustering analysis: an efficient multi-scale scheme for inelastic heterogeneous materials. Computer Methods in Applied Mechanics and Engineering 306, 319–341.

Liu, Z., Kafka, O.L., Yu, C., Liu, W.K., 2018. Data-driven self-consistent clustering analysis of heterogeneous materials with crystal plasticity. Advances in Computational Plasticity: A Book in Honour of D. Roger J. Owen , 221–242.

Liu, Z., Wu, C., Koishi, M., 2019. A deep material network for multiscale topology learning and accelerated nonlinear modeling of heterogeneous materials. Computer Methods in Applied Mechanics and Engineering 345, 1138–1168.

Masi, F., Stefanou, I., 2022. Multiscale modeling of inelastic materials with thermodynamics-based artificial neural networks (tann). Computer Methods in Applied Mechanics and Engineering 398, 115190.

Masi, F., Stefanou, I., Vannucci, P., Maffi-Berthier, V., 2021. Thermodynamics-based artificial neural networks for constitutive modeling. Journal of the Mechanics and Physics of Solids 147, 104277.

Metoui, S., Pruliere, E., Ammar, A., Dau, F., Iordanoff, I., 2018. A multiscale separated representation to compute the mechanical behavior of composites with periodic microstructure. Mathematics and Computers in Simulation 144, 162–181.

Morgan, D., Jacobs, R., 2020. Opportunities and challenges for machine

learning in materials science. Annual Review of Materials Research 50, 71–103.

Moulinec, H., Suquet, P., 1998. A numerical method for computing the overall response of nonlinear composites with complex microstructure. Computer methods in applied mechanics and engineering 157, 69–94.

Öchsner, A., 2021. Foundations of classical laminate theory. Springer.

Praud, F., 2018. Multi-scale modelling of thermoplastic-based woven composites, cyclic and time-dependent behaviour. Ph.D. thesis. Paris, ENSAM.

Praud, F., Chatzigeorgiou, G., Bikard, J., Meraghni, F., 2017a. Phenomenological multi-mechanisms constitutive modelling for thermoplastic polymers, implicit implementation and experimental validation. Mechanics of Materials 114, 9–29.

Praud, F., Chatzigeorgiou, G., Chemisky, Y., Meraghni, F., 2017b. Hybrid micromechanical-phenomenological modelling of anisotropic damage and anelasticity induced by micro-cracks in unidirectional composites. Composite Structures 182, 223–236.

Praud, F., Chatzigeorgiou, G., Meraghni, F., 2021. Fully integrated multiscale modelling of damage and time-dependency in thermoplastic-based woven composites. International Journal of Damage Mechanics 30, 163–195.

Salehi, H., Burgueño, R., 2018. Emerging artificial intelligence methods in structural engineering. Engineering structures 171, 170–189.

Strong, A.B., 2008. Fundamentals of composites manufacturing: materials, methods and applications. Society of manufacturing engineers.

Suquet, P., 1987. Elements of homogenization for inelastic solid mechanics. Homogenization techniques for composite media .

Tikarrouchine, E., Benaarbia, A., Chatzigeorgiou, G., Meraghni, F., 2021. Non-linear fe^2 multiscale simulation of damage, micro and macroscopic strains in polyamide 66-woven composite structures: Analysis and experimental validation. Composite Structures 255, 112926.

Tikarrouchine, E., Chatzigeorgiou, G., Praud, F., Piotrowski, B., Chemisky, Y., Meraghni, F., 2018. Three-dimensional fe^2 method for the simulation of non-linear, rate-dependent response of composite structures. Composite Structures 193, 165–179.

Wei, J., Chu, X., Sun, X.Y., Xu, K., Deng, H.X., Chen, J., Wei, Z., Lei, M., 2019. Machine learning in materials science. InfoMat 1, 338–358.

Wu, J., Jiang, J., Chen, Q., Chatzigeorgiou, G., Meraghni, F., 2023. Deep homogenization networks for elastic heterogeneous materials with two-and three-dimensional periodicity. International Journal of Solids and Structures , 112521.

Wu, L., Kilingar, N.G., Noels, L., et al., 2020. A recurrent neural network-accelerated multi-scale model for elasto-plastic heterogeneous materials subjected to random cyclic and non-proportional loading paths. Computer Methods in Applied Mechanics and Engineering 369, 113234.

Xu, Y., Liu, X., Cao, X., Huang, C., Liu, E., Qian, S., Liu, X., Wu, Y., Dong, F., Qiu, C.W., et al., 2021. Artificial intelligence: A powerful paradigm for scientific research. The Innovation 2.

Statement of Novelty (To the best of your knowledge, does any existing work (either submitted or already published, including

Statement of Novelty

To the best of our knowledge, there is no existing work, whether submitted or already published, including our own, that significantly overlaps with the content and findings presented in this paper. Our work represents an original contribution to the field, and we believe it introduces novel insights and methodologies that have not been previously explored.

Highlights:

- Physically informed MuTINN model by thermodynamic quantities as ISVs at the macroscale
- Thermodynamic MuTINN's foundation enhancing prediction reliability and admissibility.
- MuTINN association with a FE code towards microstructure simulations of structuress.
- Fast and frugal two-scale structural simulations through the FE-MuTINN approach.

CRediT authorship contribution statement

M. El Fallaki Idrissi: Conceptualization, Writing– Original draft, Formal analysis, Investigation, Methodology, Validation.

F. Praud: Conceptualization, Methodology, Investigation, Review & editing.

F. Meraghni: Conceptualization, Methodology, Formal analysis, Investigation, Writing- review & editing, Project administration.

F. Chinesta: Conceptualization, Methodology, Formal analysis, Investigation, Review & editing.

G. Chatzigeorgiou: Review & editing, Investigation, Methodology.

Declaration of interest statement

The authors declare that they have no known competing financial interests or personal relationships that could have appeared to influence the work reported in this paper.